# LOW TEMPERATURE THERMAL HISTORY OF MAINLAND NOVA SCOTIA USING APATITE AND ZIRCON (U-TH)/HE THERMOCHRONOLOGY

Carolina Chang

SUMBITTED IN PARTIAL FULFILLMENT OF THE REQUIREMENTS FOR THE DEGREE OF BACHELOR OF SCIENCES, HONOURS

DEPARTMENT OF EARTH SICENCES DALHOUSIE UNIVERSITY, HALIFAX, NOVA SCOTIA

MARCH 2017

# Distribution License

DalSpace requires agreement to this non-exclusive distribution license before your item can appear on DalSpace.

NON-EXCLUSIVE DISTRIBUTION LICENSE

You (the author(s) or copyright owner) grant to Dalhousie University the non-exclusive right to reproduce and distribute your submission worldwide in any medium.

You agree that Dalhousie University may, without changing the content, reformat the submission for the purpose of preservation.

You also agree that Dalhousie University may keep more than one copy of this submission for purposes of security, back-up and preservation.

You agree that the submission is your original work, and that you have the right to grant the rights contained in this license. You also agree that your submission does not, to the best of your knowledge, infringe upon anyone's copyright.

If the submission contains material for which you do not hold copyright, you agree that you have obtained the unrestricted permission of the copyright owner to grant Dalhousie University the rights required by this license, and that such third-party owned material is clearly identified and acknowledged within the text or content of the submission.

If the submission is based upon work that has been sponsored or supported by an agency or organization other than Dalhousie University, you assert that you have fulfilled any right of review or other obligations required by such contract or agreement.

Dalhousie University will clearly identify your name(s) as the author(s) or owner(s) of the submission, and will not make any alteration to the content of the files that you have submitted.

If you have questions regarding this license please contact the repository manager at dalspace@dal.ca.

Grant the distribution license by signing and dating below.

_____ _____

Name of signatory Date

DALHOUSIE UNIVERSITY

**Department of Earth Sciences**
Halifax, Nova Scotia
Canada B3H 4R2
(902) 494-2358

DATE: 28 April 2017

AUTHOR: CAROLINA CHANG

TITLE: LOW TEMPERATURE THERMAL HISTORY OF MAINLAND NOVA SCOTIA USING APATITE AND ZIRCON (U-TH)/HE THERMOCHRONOLOGY

Degree: B. Sc. Honours Earth Sciences Convocation: May Year: 2017

**Abstract**

Passive margins are the transition between continental and oceanic crust. Their formation begins with continental rifting, sedimentation in the syn-rift basins, may include magmatic sequences, and seafloor spreading at which point the faults are no longer active and the margin is considered passive. During the supercontinent configuration of Pangaea, Nova Scotia was sutured to Morocco and began to rift apart in the late Triassic and separated by the early-mid Jurassic, when the margin became passive and the Atlantic Ocean began to open.

Recently, investigation of structural relationships and low temperature thermochronology in passive margins has revealed that there are in fact reactivated faults at multiple localities on the Atlantic margins; of interest for this project is the Nova Scotian and US margin where km-scale post-rift vertical movements are observed. In comparison to the US, the Scotian margin has a largely subdued topography and represents the transition from volcanic margin to the south and non-volcanic to the north. Cooling ages in the New England White Mountains obtained using apatite fission track analysis yield Cretaceous ages that researchers propose may be a result of small scale asthenospheric convection or changing orientation of seafloor spreading. In Nova Scotia, cooling ages are Triassic and Jurassic. Differences between the two proximal margins raise the question of what processes are responsible for their respective ages and whether those processes take place in both the US and Scotian margin. The US margin can be used as a valuable comparison since it has been more extensively investigated compared to the Canadian extension.

The objective of this project is to constrain the thermal history of southern mainland Nova Scotia using apatite and zircon (U-Th)/He analysis, which yields the age at which a sample cooled beyond ~70 ˚C and 185 ˚C, respectively. Five bedrock samples collected revealed cooling beyond 185 ˚C occurred at 220 Ma and beyond 70 ˚C at 188.4 Ma. Cooling rates are one order of magnitude greater during cooling from 185 – 70 ˚C than 70 ˚C to mean surface temperature, suggesting Nova Scotia's low temperature thermal history is dominated by post-rift erosion unlike the US passive margin.

**Keywords**: Thermochronology, Nova Scotia, passive margin, (U-Th)/He analysis

## Contents

## Table of Figures

## List of Tables

**Acknowledgements**

I would like to thank my supervisor Isabelle Coutand for her scientific guidance, and also for inspiring me in Introduction to Geology to pursue this field of study. Additionally, I would like to thank Roman Kislitsyn from Dalhousie's Noble Gas Lab and Bertha Louis for dedicating the time to answering my seemingly endless technical questions and teaching me the tedious art of mineral separation and sample preparation. I would also like to thank the Shell Experiential Learning Fund, which funded the analytical work of this thesis.

I have to thank my parents to whom I am incredibly grateful, having worked harder than I could imagine to provide me with this education and have always supported my learning. To Pablo and Cristina, thank you for paving the way and being great role models.

Lastly, a big thank you to the incredible friends that have put up with me this year, and Mike Young for the endless encouragement.

# Chapter 1: Introduction

## 1.1 Passive Margins

Passive margins are located at the transition between continental and oceanic lithosphere and consist of asymmetric normal faulted rift basins filled with syn-rift clastic sediment and salt deposits, overlain by post rift sediments (Nemčok 2016). The formation of passive margins begins with continental rifting, continental breakup, nucleation of an oceanic ridge, and ensuing sea-floor spreading, a stage during which the syn-rift normal faults are no longer active converting the active rifting margin into a passive margin.

Initiation of rifting occurs where weak zones are present in stiff continental lithosphere and localized thinning and weakening (i.e. necking instabilities) can develop (Chenin and Beaumont 2013). A continental rift's width, magmatism, thermal subsidence, and flexural uplift are all strongly influenced by lithology, thermal state, and inherited structural features in the continental lithosphere (Chenin and Beaumont 2013, Huismans and Beaumont 2014, Peterson and Schiffer 2016) resulting in different types of passive margins. Huismans and Beaumont (2014) modelled two end-member continental rifting styles differentiated by whether the rheology of the lithosphere is stiff or plastic and whether the crust and the upper mantle are decoupled. Figure 1 illustrates differences between Type-I rifts (1a) where the continental lithosphere is stiff and there is a strong coupling between rheological layers, while Type-II rifts (1b) have weak crustal layers that allow for decoupling during extension.

Type-I margins are non-volcanic and are distinguished by (Figure 1a): 1) the development of major basin forming normal faults that penetrate at least into the crust, 2) narrow transition zones (<100 km) where continental crust thins abruptly, 3) asymmetric geometry and uplift of rift flanks, 4) breakup of crust precedes breakup of mantle, 5) exhumation and exposure or near exposure of serpentinized sub-continental lithospheric mantle (SCLM) at the transition between continental and oceanic crust, 6) relatively little

surface magmatism during rifting, 7) initially thin oceanic crust and late-stage development of a magmatic spreading centre (Huismans and Beaumont 2014).

Pliable lithosphere forms Type-II margins (Figure 1b) which characteristically have a) ultra-wide (>350 km) regions of thinned continental crust with little evidence of a lower crustal layer, b) early syn-rift sedimentary basins, c) undeformed late syn-rift sediments and salt diapirism in some instances, d) shallow marine or lacustrine-fluvial sediments in syn-rift sag basins likely formed by e) SCLM replaced by hot asthenosphere beneath large regions of the margin, f) lack of mechanical flexure flank uplift, g) no clear evidence of exhumed mantle lithosphere, h) limited magmatism during rifting, magmatic underplating and seaward dipping reflectors in some cases, i) a mature magmatic mid ocean ridge established soon after crustal breakup (Huismans and Beaumont 2014).

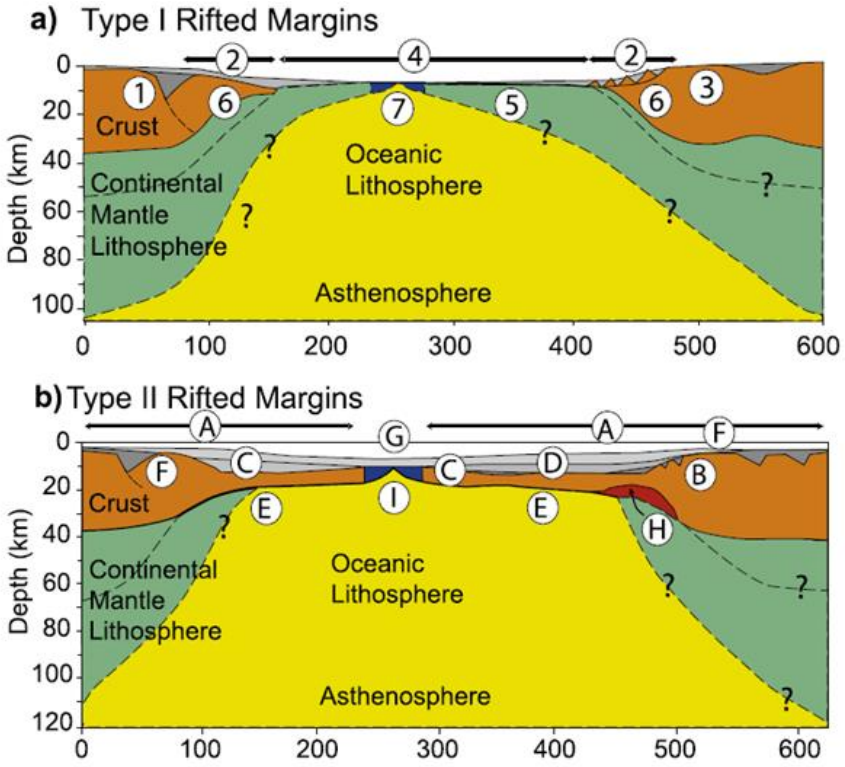


Figure 1: Schematic diagram illustrating characteristic properties of Type-I (a) and Type-II (b) rifting styles from Huismans and Beaumont (2014).

In addition to outlining end-member characteristics, Huismans and Beaumont (2014) offer templates of Type-I and Type- II sedimentary basins for determining the rifting style using basin attributes, implying upper crustal morphology is strongly influenced by lithospheric processes. Previous research focuses on the interaction between tectonics and surface processes, and investigates the relationship between rifting and denudation (Pazzaglia and Gardner 1994, Beaumont et al. 2000, Spotila 2004). Vertical movements and thermal evolution of passive margins condition the nature and thickness of the sedimentary sequence preserved on these margins and their high potential for the presence of petroleum reservoirs is of economic interest for oil industry.

### 1.2 Central Atlantic Margin

The Central Atlantic Margin (Figure 2) represents the rifted margin resulting from the opening of the Atlantic Ocean ~170 Ma ago (Withjack et al. 1995). Figure 3a illustrates the approximate configuration of northwest Africa and eastern North America in the Late Paleozoic with NE-SW oriented faults inherited from Pangaea's accretion. The onset of continental extension reactivated and inverted contractional features throughout the rift system forming syn-rift basins (Figure 3b). Despite their geographical close proximity, the Nova Scotian and Central United States (US) passive margins have different characteristics in terms of topography, presence of magmatism, and crustal structure. Large escarpments (paleo-rift flanks), often associated with passive margins, are present in the US and Morocco, however, are absent along the Scotian Margin (Pazzaglia and Gardner 2000, Pazzaglia and Gardner 1994, Withjack and Schlische 2005). Further, the Scotian margin marks the transition from volcanic rifting to the south of Nova Scotia and non-volcanic to the north, East of Cape Breton (Figure 4, Keen and Potter 1995). A volcanic margin differs from non-volcanic in that it breaks up over a hotter mantle and exhibits a shorter margin width (Geoffroy 2005). Distinct features of volcanic margins are high extension rates, forming thick oceanic crust, and faults dipping toward the continent resulting from seaward flexure of the oceanic crust. The transitional crust consists of heavily intruded continental crust with seaward dipping reflector (SDR) sequences of flood

basalt and tuff (Geoffroy 2005). The presence of SDR causes magnetic anomalies, which act as good markers for determining the type of rifted margin.

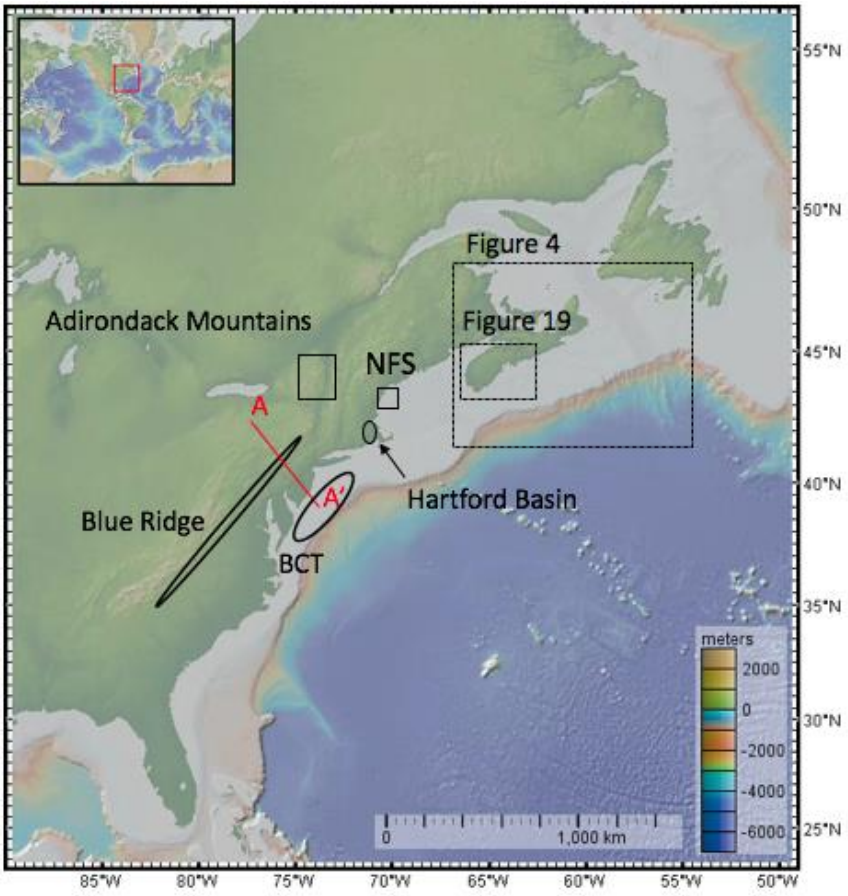


Figure 2: Map of eastern center Atlantic passive margin (from GeoMapApp). BCT is the Baltimore Canyon Trough, NFS is the strike-slip Norumbega Fault System, A-A' line is the cross section in Figure 7.

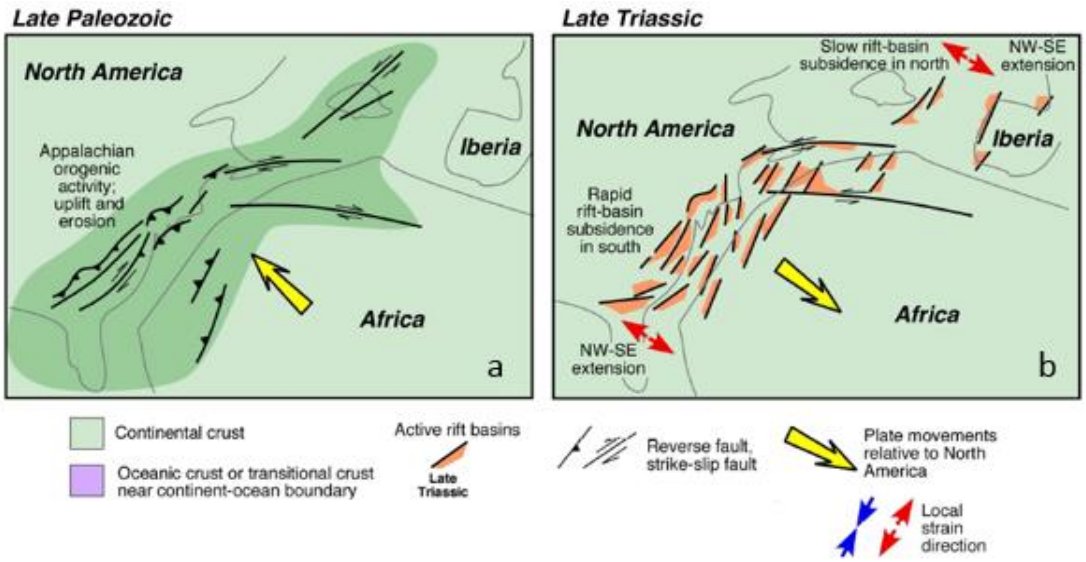


Figure 3: Cartoon showing tectonic evolution of the North American rift system illustrating (a) pre-rift faults resulting from Paleozoic Appalachian orogeny (b) and the Late Triassic configuration at the onset of continental extension and subsequent rift- basins (Withjack and Schlische 2005).

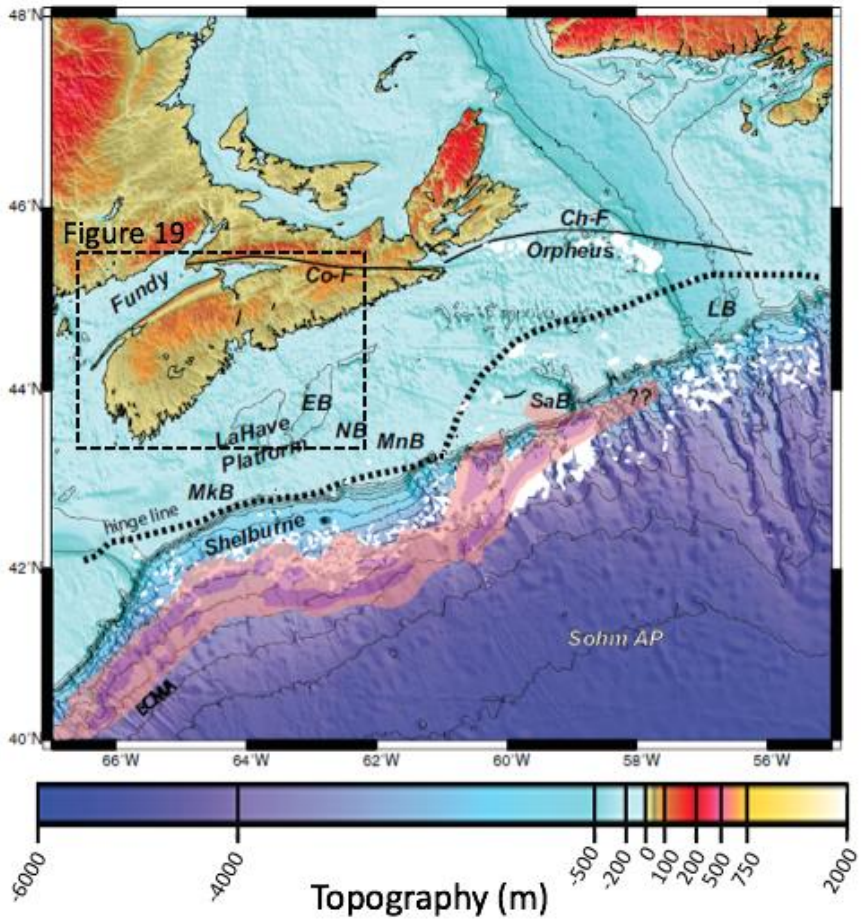


Figure 4: Bathymetry and topography of the Nova Scotia margin with abbreviations of major basins: MkB: Mohawk, EB: Emerald, NB:Naskapi, MnB:Mohican, SaB: Sable, LB: Laurentian. The East Coast Magnetic Anomaly (ECMA) is marked in pink and purple, salt structures in white, hinge line is a dotted black line, two major faults: Cobequid (Co-F) and Chedabucto (Ch-F), and the abyssal plain: AP, after Louden et al. (2013).

Consistent with the wide margin expected from a non-volcanic margin, the Scotian margin has a wider extension zone than in the US margin, with its continental crust thinning over a distance of 200 km (Keen and Potter 1995). Geodynamic variation between the US and southern Canada has topographic expressions such as the Blue Ridge Escarpment along the eastern US margin (Figure 2) which is considered forming from an initial rift flank (Pazzaglia and Gardner 2000), and which is absent to the north. Pazzaglia and Gardner (1994) use geodynamic and erosional models to propose that the elevated topography is a product of increased

sediment source flux from decreased sea level and subsequent sediment loading in an offshore basin causing onshore flexure. Apatite (U-Th)/He (AHe) and apatite fission track (AFT) cooling ages along the northern US margin are mid Jurassic to Cretaceous and reflect incision, thermal anomalies, and fault reactivation (Roden-Tice and Wintsch 2002, Taylor and Fitzgerald 2011, West et al. 2008). Spotila et al. (2004) investigated the Blue Ridge Escarpment and found AHe ages ranging from 204 - 102 Ma on the upland and ages along the piedmont from 108 – 68 Ma, decreasing in age towards the coast. Such transects do not currently exist in Nova Scotia.

There are, however, a number of low-temperature thermochronological ages including (U-Th)/He and fission-track on apatite crystals (AHe and AFT, respectively), on mainland collected by Grist and Zentilli (2003). AHe ages range from 209 - 182 Ma and AFT ages bordering the Bay of Fundy from 244 – 210 Ma, corresponding to the continental rifting. However thermal modeling using these data have produced Time-temperature paths poorly predicting the measured AHe ages. It was then suggested that these model predictions could be explained by a combination of decreased post-Paleocene exhumational cooling and decreased eustatic sea level (Grist and Zentilli 2003).

In addition to processes associated with passive margin development, Nova Scotia's surface morphology has been impacted by Quaternary glaciations as evidenced by the occurrence of glacially striated continental bedrock, tills, and varved lacustrine deposits (Peters 2009, Stea et al. 1998). The maximum extent of glaciation provided in a model by Stea et al. (1998) is situated at the Scotian slope and the minimum extent near the coastline. Retreat of the Laurentide ice sheet ~13.5 Ka (Stea and Mott 1997) coupled with glacial erosion could have impacted Nova Scotia's continental crust, thermal/erosional and surface uplift history if ice unloading induced significant isostatic rebound and crustal denudation.

### 1.3 Research Objectives

Preliminary thermochronological studies conducted along the Scotian margin have not been spatially systematic and have yielded conflicting results as to which processes drive post-

Cretaceous exhumation there. This study is part of an ongoing effort aiming at quantifying at high spatial and temporal resolution the extent and rate of upper crustal exhumation of mainland Nova Scotia. The specific objectives of this study are to:

1) Constrain the thermal history in our study area using low-temperature multi-thermochronometry.

2) Complement with preliminary results obtained in Nova Scotia and compare with thermochronological results published for the eastern US.

### 1.4 Tools

Low-temperature thermochronology including apatite and zircon (U-Th)/He are radiometric methods well-suited methods for onshore studies of denudation because their closure temperature correspond to the upper few kilometres of the crust.

Thermochronological methods exploit the spontaneous decay of radioactive isotopes and allow us to calculate the time at which a rock sample cooled beyond a range of effective closure temperatures (Reiners and Brandon 2006). (U-Th)/He dating relies on the spontaneous decay of uranium of $^{238}U$, $^{235}U$, $^{232}Th$, and $^{147}Sm$, producing daughter products ($^{4}He$), referred to as alpha particles, at a known rate. The effective closure temperatures, which is the temperature below which > 90% of the daughter products do not diffuse out of the crystals are ~ 70 ˚C and ~185 ˚C for apatite and zircon, respectively (Reiners and Brandon 2006, Wolfe and Stockli 2010). By determining the concentration of $^{4}He$ and parent isotope present in each crystal, a cooling age can be calculated. These data are then used to calculate cooling rate and converted to exhumation rate with knowledge of the geothermal gradient.

### 1.5 Expected Outcomes

Cooling ages may reflect 1) tectonic exhumation associated with continental rifting, 2) post-rift shortening observed by Withjack and Schlische (2005) in the Fundy Basin in Nova Scotia as well as the Taylorsville and Richmond Basins in the US, 3) Cenozoic ages may suggest that a scenario

like that on the US margin across the Baltimore Canyon Trough (Figure 7) where offshore sediment loading contributes to flexure onshore, 4) Quaternary age would indicate that deglaciation of the Laurentide ice sheet has produced sufficient rock uplift to generate km-scale denudation.

# Chapter 2: Geologic Background

## 2.1 Introduction

In this chapter, we introduce the geology of the Nova Scotia's passive margin, as well as its southern continuation in the US (Figure 2). The tectonic history of the margins is discussed, followed by a review of existing thermochronologic studies.

## 2.2 Geology of Nova Scotia

### 2.2.1 Pre-rifting period (pre-Late Triassic)

Nova Scotia is located on the southeast coast of Canada and marks the northern extent of the Appalachian range. The province consists of two geologic terranes separated by the Cobequid Chedabucto Fault Zone (CCFZ): Avalon and Meguma (Figure 4). South of the CCFZ, the Meguma Terrane is dominated by the Meguma Supergroup consisting of a lower meta-sandstone Goldenville Group overlain by Halifax Group slates, both being turbiditic sequences deposited in abyssal plain and continental rise during the Cambrian and lower Ordovician (Waldron et al. 2009). A third to half of mainland southern Nova Scotia is intruded by the South Mountain Batholith (SMB), a syn-orogenic peraluminous granodiorite formed during the Acadian orogeny in the Devonian (Mckenzie and Clarke 1975). Upon emplacement, the SMB has caused contact metamorphism throughout much of the Meguma Terrane (Jamieson et al. 2012, Gibling 1995).

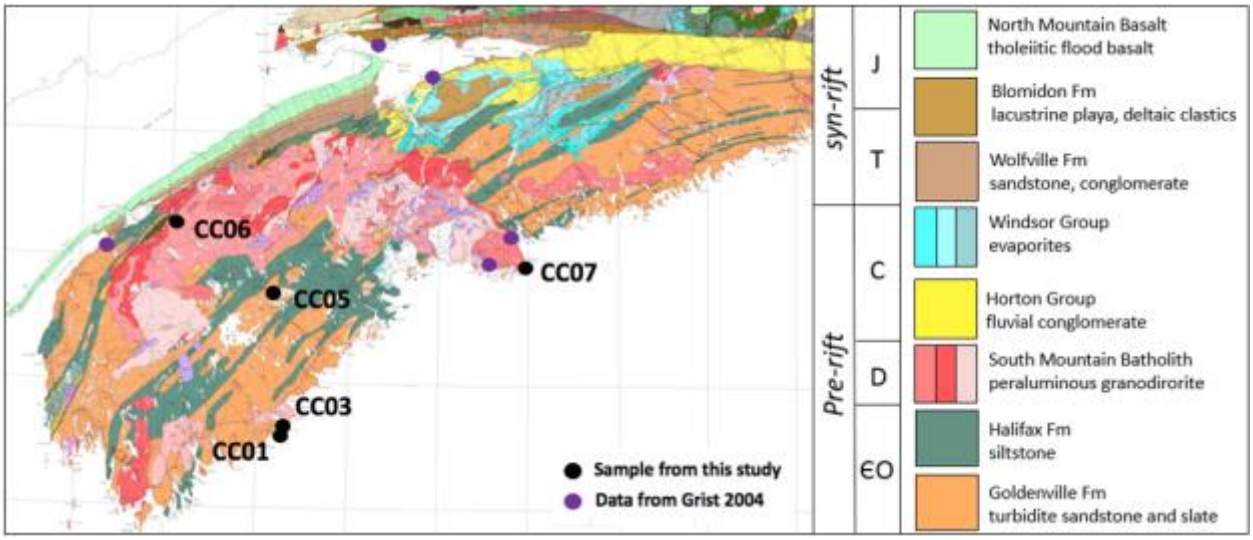


Figure 5: Geologic map of mainland Nova Scotia where black circles are sample locations from this study and purple circles are those from Grist (2004). The simplified bedrock geology legend differentiates pre-rift from syn-rift lithologies (White 2012).

To the north of the CCFZ, the Avalon Terrane consists of slabs accreted during the Appalachian orogeny, which sutured Nova Scotia and present day western Morocco (Barr and Raeside 1989, Dehler 2012). The Ordovician Taconic, Devonian-Silurian Acadian, and Permian Alleghenian orogenies are grouped as the 'Appalachian orogeny', which altogether, closed the Rheic Ocean and subsequently formed Pangaea (Hatcher 2010). Extensive deformation took place in Nova Scotia during the Acadian Orogeny from mid to late Devonian generating pluri-kilometric isoclinal folds characterized by SW-NE trending axial planes; whereas, Taconic and Alleghanian orogenic effects are not regional scale (Mckenzie and Clarke 1975). The Carboniferous times are marked by the deposition of alluvial clastics and evaporites of the Horton and Windsor Group (Figure 5) in a shallow marine environment under hot and dry climate, capturing the palaeo-equatorial location of Nova Scotia prior to rifting (Gibling et al. 2008). The Permian is effectively eroded from mainland Nova Scotia and the strata overlying the Carboniferous sedimentary units consists of syn-rift sediments.

### 2.2.2 Syn-rifting period (late Triassic to middle Jurassic)

Rifting between central North America and northwestern Africa began in the late Triassic in the rocks of the Appalachian orogeny (Keen and Potter 1995). NW-SE oriented extensional deformation has reactivated Paleozoic contractional structures inherited from Pangaea's accretion and consequently formed asymmetric normal faults (Withjack et al. 1995). Based on seismic lines on the offshore margin, Keen and Potter (1995) report 100 km of very thin transitional or continental crust under the slope and rise, which can be satisfied with stretching factors of 2-3 (Keen and Potter 1995). Syn-rift basins currently located on the Scotian shelf, slope, and rise, are filled with up to 15-km- thick syn-rift sediments (Keen and Potter 1995). These include the syn-rift Fundy Group, which consists of continental deposits dominated by eolian, alluvial fan and braided stream sedimentary facies with evidences of caliche paleosols indicative of an arid climate in the Fundy Basin area during the Triassic (Hubert and Mertz 2006). Due to the warm and arid conditions, shallow seas repeatedly evaporated and thick salt deposits up to 3 km formed the Jurassic Argo Formation, preserved on the Scotian Shelf (Jansa and Wade 1975). In the Scotian Basin, the Argo Formation interfingers lower Jurassic redbeds of the Eurydice Fm (Jansa and Wade 1975). The Mid-Jurassic enters a base level fall and deposits shales and sandstones of the Mohican formation and dolostones of the Iroquois Formation (Jansa and Wade 1975).

Flood basalts, dykes, and sills crosscutting or interlayered within the syn-rift strata belong to Central Atlantic Magmatic Province (CAMP, Kontak and Archibald 2003), a magmatic episode rapidly emplaced ~200 Ma ago and present in Canada, US, South America, southern Europe, and NW Africa (Melankholin and Sushchevskya 2015, Withjack and Schlische 2005). In Nova Scotia, the most prominent expression of CAMP is the North Mountain Basalt (NMB) located along the southern shore of the Bay of Fundy, which stratigraphically overlies the red beds of the Triassic-Jurassic Blomindon (Figure 5, Kontak and Archibald 2003). The NMB is interpreted as being a relict of the failed rift between mainland Nova Scotia and New Brunswick

with a whole-rock $^{40}Ar/^{39}Ar$ age 201.0 ± 2.5 Ma, at the Triassic-Jurassic boundary (Kontak and Archibald 2003).

Following CAMP magmatism is the formation of seaward dipping reflectors (SDR) characteristic of a phase of productive volcanism in the early stages of rifting (discussed in Chapter 1**: Introduction**; Geoffroy 2005). The thickness of SDR as measured by the strength of the East Coast Magnetic Anomaly (ECMA), seen in Figure 4 as a purple sub-linear feature offshore (Keen and Potter 1995). Southern Nova Scotia marks the gradual transition from a volcanic margin in the US, into a non-volcanic margin, evidenced by weakening ECMA northwards and the absence of ECMA and SDR in the North Atlantic Margin (Dehler 2012). Jurassic SDRs can be seen identified in seismic profiles structured as a fanning wedge with reflectors dipping eastward at 5° at the top and 15-20° at the base (Keen and Potter 1995). Wide extension zones, such as that of the Scotian Margin, are characteristic of colder rifting where strain localizes comparatively slowly; whereas, narrow extension zones resulting from hot rifts allows strain to localize quickly and asthenospheric upwelling causes decompression melting (Van Avendonk et al. 2008). Along-strike studies into the US margin shows progressive narrowing of the extension zone (Keen et al. 1995).

### 2.2.3 Post-rifting period (Middle Jurassic to Present)

Syn-rift strata in Nova Scotia are overlain by a relatively thin cover related to minimal subsidence (Van Avendonk 2009). The post-rift Cretaceous Chaswood formation unconformably overlies the Carboniferous Windsor Group and is overlain by Quaternary sediments (Stea and Pullan 2001). It consists of terrestrial clastic sediments, dominated by quartzose sand and kaolinitic clays, with a 90-170 m thickness (Stea and Pullan 2001). Post-rift subsidence is a common feature in rifted environments, but the lack of significant subsidence at the Scotian margin leads Keen and Potter (1995) to suggest the formation of rift basins are predominantly attributed to crustal deformation rather than lithospheric mantle involvement.

Withjack et al. (1995) report shortening in the N-S to NE-SW direction evidenced by NE-striking anticlines in the hanging walls of border faults in the Fundy Basin. Proceeding Jurassic sedimentation, but before the early Cretaceous, compression caused reactivation of Paleozoic contractional structures and inverting extensional features (Withjack et al. 1995). Post-rift shortening remains enigmatic, but it is possible that ridge-push and initial continental resistance to plate motion at the onset of seafloor spreading could cause shortening and inversion in passive margins (Withjack and Schlische 2005).

Salt diapirism can also trigger deformation by tilting or differential sediment loading (Allen and Beaumont 2016). On the Scotian Margin, salt bodies moved seaward and vertically; the Argo Fm rose up to 10 km as diapirs into overlying strata (Jansa and Wade 1975). In the offshore Jeanne d'Arc basin east of Newfoundland, salt propagation folds formed from fault termination at the base of thick salt deposits (Withjack and Schlische 2005).

### 2.2.4 Low-temperature thermochronology on mainland Nova Scotia

AHe and AFT age data are already available in some locations of our study area (Grist and Zentilli, 2003; for data location, see Figure 5).

AHe age data available in on a SMB sample in Halifax (Figure 20, sample HA), yielded ages of 208.5 ± 16.7 Ma and 204.6 ± 16.4 Ma and towards the southwest in Mahone Bay, two samples yielded ages of 202.9 ± 16.2 Ma and 147.9 Ma. Besides the last sample, these age data are remarkably reproducible, yet, each are determined by a single-grain age or the mean of two single-grain ages. Currently, between three to five aliquots are required for this kind of analysis, to produce statistically meaningful cooling ages.

AFT age data are available on the Bay of Fundy at Rainy Cove, Partridge Island, and Digby and yielded ages 244 ± 144.4 Ma, 239 ± 18 Ma and 210 ± 18 Ma, respectively (locations on Figure 5). The sample from Digby was collected at 60-meters-depth from a drill core from which Grist (2004) also analyzed other samples down to a depth of 1400 m, and from which they were able to determine ~ 15 °C/Km geotherm since 250 Ma.

Temperature-time models constrained with these AFT data suggest the samples cooled from temperatures > 120 °C in the late Jurassic and late Cretaceous to Paleocene (Grist and Zentilli, 2003), then experience reheating at about 200 Ma, cooling down to temperature of about 20 °C at around 110 Ma then heating again to finally experience 25-30 °C of post-Paleocene cooling attributed to a decrease in eustatic sea level, which induced up to ~700 m of continental erosion resulting in 13 °C of exhumational cooling (Grist and Zentilli 2003). Grist (2004) also used AHe to constrain these model predictions, however their measured ages are not consistent with the ages predicted by the model. The (U-Th)/He predicted ages from AFT modelling would require that maximum post-Jurassic temperatures of the sample never exceeded 50 °C, which is not the case.

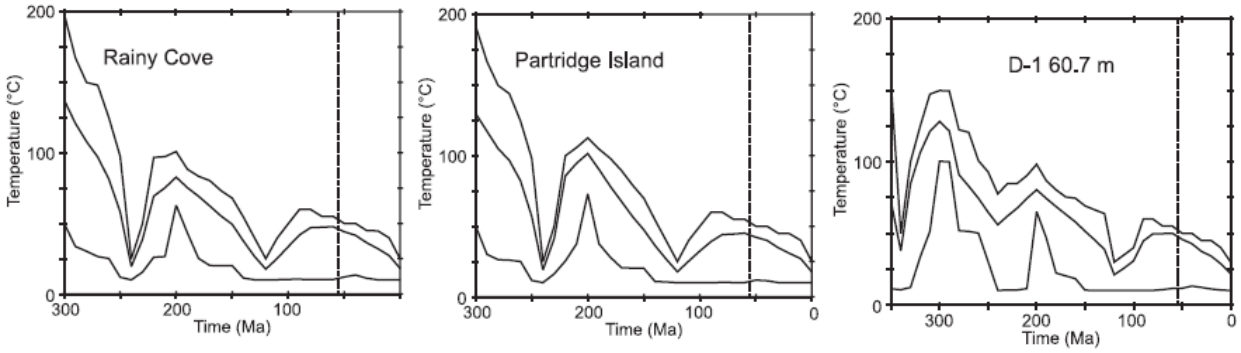


Figure 6: Temperature-time models for the Rainy Cove, Partridge Island, and Digby (D-1 60-7 m) samples. The vertical black dashed line indicates the end of the Paleocene (55 Ma) (after Grist and Zentilli 2003).

## 2.3 US Passive Margin

The US passive margin is located along the east coast and is the along-strike southern continuation of the Scotian margin (Figure 2). The US margin has been investigated more extensively than the northern counterpart and has a dense set of (U-Th)/He and fission track data to which we can compare cooling ages from the Scotian margin. Further, the US margin exhibits significant topography as compared to the largely subdued Nova Scotia raising the question as to what are the different processes that form these contrasted geomorphological

features. For this study, we focus on the US passive margin from Maine in the north to Maryland in the south.

### 2.3.1 Evolution of US margin

Much like Nova Scotia, the US passive margin has experienced overprinting of orogenic deformation. Collision of Laurentia forming the supercontinent Rodinia caused the Grenville orogeny in the Proterozoic (Rivers 1996). Rodinia existed for ~150 Ma (Li et al. 2008), rifted, and subsequently amalgamated into Pangaea by the Permian, when the Taconic, Acadian, and Alleghenian orogenies, closed the Rheic Ocean (Hatcher 2010) forming high-grade metamorphic rocks, thrust fault systems, and km-scale relief (Taylor and Fitzgerald 2011).

### 2.3.2 Rifting

In response to NW-SE extension, rifting commenced in the late Triassic and transitioned into seafloor spreading in the early to early-mid Jurassic (Withjack et al. 2012). Syn-rift CAMP magmatism was more prevalent on the US margin but was concurrent (Withjack et al. 2013). The structure of the US margin differs from the Scotian margin in that the early post-rift formation of SDRs are up to 23 km in thickness (Pazzaglia and Gardner). This thick volcanic unit tapers near SW offshore Nova Scotia (Figure 4), causes the East Coast Magnetic anomaly's strength southward to Florida, and its termination marks the transition from a volcanic to non-volcanic rifted margin toward the north (Withjack and Schlische 2005).

Onshore, a coast-parallel, seaward facing escarpment spanning much of the US margin is the relict of rift flank uplift (Pazzaglia and Gardner 2000). Blue Ridge has an average elevation of 1000 m and generates 800 m of local relief in contrast to the Adirondacks which have over 1500 m elevation (Figure 2; Pazzaglia and Brandon 1996). Its width is 15 km in the north section in Pennsylvania and broadens to 120 km toward the south in Georgia (Pazzaglia and Gardner 2000). To the east of Blue Ridge is the Baltimore Canyon Trough (BCT; Figure 4), considered one of the most thoroughly studied basins in the US margin, spanning 400 km in length in a SW-NE direction, 18 km deep, containing over 7 km of eroded continental crust

(Poag and Sevon 1989). The cross section Figure 7 illustrates the spatial relationships between the Appalachians, the east-facing Blue Ridge Escarpment, the low-laying piedmont and coastal plain, and the BCT.

### 2.3.3 Post-rift deformation

Observations suggesting post-rift shortening is not limited to the Scotian margin and can be found on the US margin. NE striking reverse faults and folds in the Taylorsville Basin evidence NW-SE compression before the Cretaceous (Le Tourneau 1999). Based on low temperature thermochronology data, Roden-Tice and Wintsch (2002) argue that late Cretaceous normal faulting occurred in New England forming grabens that were thought to be rift-related.

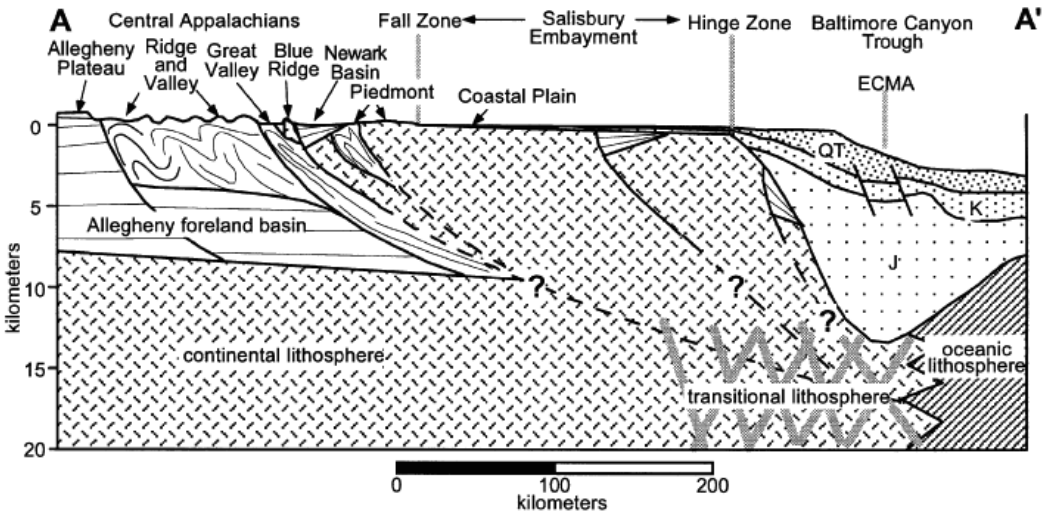


Figure 7: Cross section of the Atlantic margin from the Susquehanna Basin to Hatteras Basin (for location, see Figure 2). Abbreviations are QT = Cenozoic sediments, K = Cretaceous sediments, and J= Jurassic sediments (Pazzaglia and Brandon 1996).

### 2.2.2 Thermochronology onshore the US margin

32 Paleozoic metamorphic rock samples processed in the Hartford basin in New England (see Figure 2 for location) yielded AFT cooling ages of 168-98 Ma suggesting unroofing from late Jurassic to early Cretaceous. Zircon fission track (ZFT) with a closure temperature of ~250 ˚C

range from 238-167 Ma and along with AFT ages, gradually become younger towards the north and the west ends of the basin suggesting differential denudation, driven by normal faulting and rotation (Roden-Tice and Wintchse 2002). The juxtaposition of ~25 Ma older basin rocks compared to the basin bounding rock indicates displacement younger than the youngest AFT age of <100 Ma and therefore the basin must be younger than rifting. Roden-Tice and Wintchse (2002) argue that the basin bounding fault of the Hartford Basin in New England didn't reactivate until the Cretaceous.

In NE-SW trending Presidential Range which spans from New Hampshire to western Maine (locate on Figure 2), Roden-Tice et al. (2012) use age-elevation profiles in Mt. Washington to identify three phases of varied unroofing rates: 0.03 mm/a for 152-137 Ma, 0.01 mm/a for 137-110 Ma and 0.04 mm/a for 110-101 Ma (Figure 8) and a long-term rate of 0.02 mm/a. 173 AFT ages in the northern Adirondacks in northern New York State range from 173 - 70 Ma (Rode-Tice et al. 2012) without showing any significant exhumation gradient unlike that recorded by Roden-Tice and Wintchse 2002, Taylor and Fitzgerald 2011). The relief present in the Adirondacks has likely developed through plateau dissection during periodic base level changes (Taylor and Fitzgerald 2011).

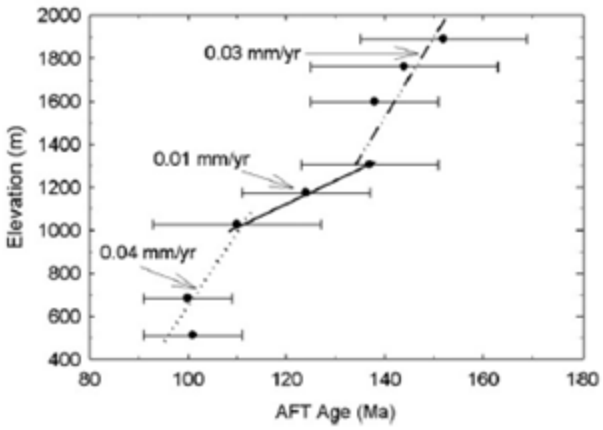


Figure 8: AFT age versus elevation from base to summit of Mt. Washington (Roden-Tice et al. 2012).

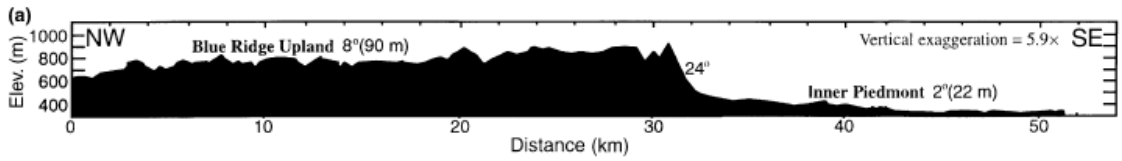


Figure 9: Elevation profile across the Blue Ridge on a NW-SE line. Slopes of the upland, escarpment and piedmont are reported as well as respective total relief in parentheses (Spotila et al. 2004).

Pazzaglia and Gardner (1994, 2000) and Pazzaglia and Brandon (1996) used geodynamic and surface process models to suggest that the topography of Blue Ridge resulted from base level drop associated with continental rifting (resulting in increased source flux), coupled with offshore sediment loading leading to a continental flexural bulge. Spotila et al. (2004) argue that flexural uplift is not large enough to generate this magnitude of relief. AHe analysis from a transect (cross section in Figure 9) across the Blue Ridge upland and the piedmont yield ages of 122-204 Ma and 68-108 Ma respectively, which supports their argument since the response to sediment loading would require younger ages (Spotila et al. 2004). Ages on the piedmont gradually decrease away from the upland suggesting the presence of a previously higher topography that experienced progressive erosion down to its current topographic level while generating sediment pulses in the BCT from the Miocene onward. The preferred explanation of Spotila et al (2004) is that this age distribution results from long-term erosional retreat of the escarpment and asymmetric divide through the Cenozoic. Younger ages on the piedmont are likely the result of both faster exhumation there and topography induced non-planar isochrons (Spotila et al. 2004).

AFT and AHe ages were collected in the strike-slip Narumba Fault System (NFS) in Maine (NFS, Figure 2) where the Acadian orogeny caused amphibolite facies metamorphism and experienced subsequent intrusion by Siluran to late Pennsylvanian plutons (West et al. 2008). AFT models with data across the fault zone indicate slow cooling of 0.5-1 ˚C/Ma between 160-

80 ˚C from late Jurassic to late Cretaceous and 0.1-0.4 ˚C/Ma between 70 – 50 Ma during the late Cretaceous (West et al. 2008).

## Chapter 3: Methods

### 3.1 Low Temperature Thermochronology

Low temperature thermochronology consists of a set of radiometric methods, which allow for the reconstruction of thermal histories of rock samples. Historically, assigning an age to extensional events required the dating of intrusive or extrusive rocks or sediments emplaced/deposited before and after tectonism or dating strata (Stockli 2005). However, erosion associated with tectonics frequently leaves too few datable markers to reconstruct the geological history, this is where thermochronology becomes a powerful approach to directly date crustal rock cooling related to tectonically-driven exhumation (Stockli 2005). The temperature sensitivity of (U-Th)/He and apatite fission track systems compared to other thermochronometers (Figure 10) allow us to investigate processes occurring in the upper 1-5 km of the crust assuming a mean annual surface temperature of 10 ± 5 ˚C and average geothermal gradient 25 ˚C/km.

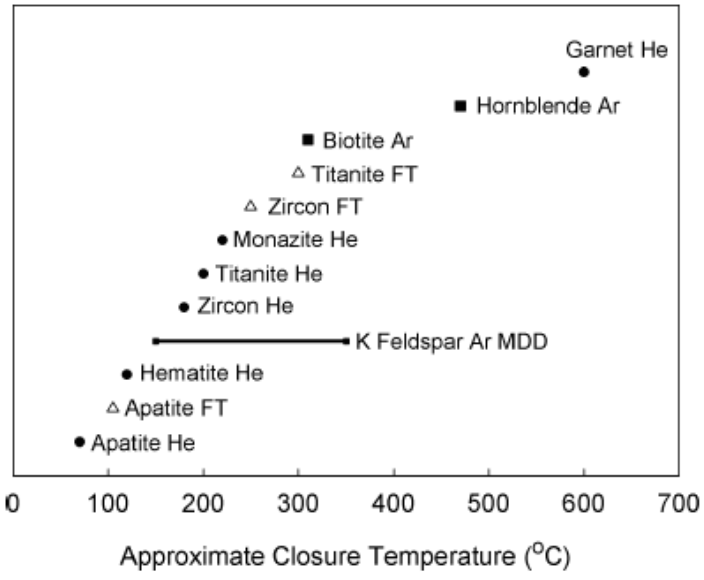


Figure 10: Closure temperatures of various thermochronometers (Farley 2002)

The premise of (U-Th)/He and fission track dating methods is the spontaneous decay of radioactive isotopes which occur at known rates and whose daughter products are retained below their respective closure temperatures. By measuring their parent and daughter products, the age at which the sample cooled beyond a particular range of temperature can be determined, with some assumptions discussed in this chapter.

## 3.2 (U-Th)/He dating

### 3.2.1 U, Th, and Sm isotopes

The (U-Th)/He dating method uses the progressive decay of $^{238}U$, $^{235}U$, $^{232}Th$, and $^{147}Sm$ (for apatite only), which produces $^{4}He$, also called α particles. $^{238}U$, $^{235}U$, and $^{232}Th$ produce 8, 7, and 6 α particles, through their decay chain toward stable elements $^{206}Pb$, $^{207}Pb$ and $^{208}Pb$, respectively (Figure 11) while $^{147}Sm$ produces one α particle as it decays to $^{143}Nd$.

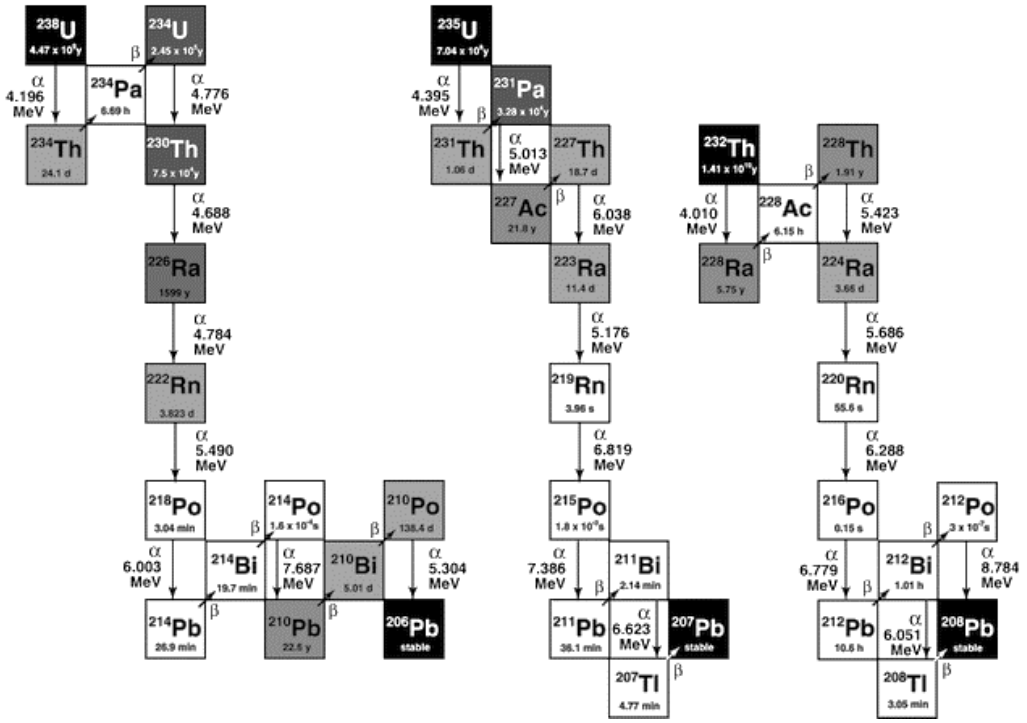


Figure 11: Decay chains of $^{238}U$, $^{235}U$ and $^{232}U$ showing progressive α and ß decay in vertical and horizontal reactions, respectively ending with stable $^{206}Pb$, $^{207}Pb$, and $^{208}Pb$ (image from The Royal Society of Chemistry).

### 3.2.2 $^4$He Behaviour: ingrowth and diffusivity

$^4$He ingrowth is captured by the equation (Farley and Stockli 2002):

$$\frac{d^4He}{dt} = 8\lambda_{235}{}^{235}U + 6\lambda_{232}{}^{232}Th + \lambda_{147}{}^{147}Sm \qquad \text{Equation 1}$$

Where λ is the decay constant for the given decay chain and $^{238}$U, $^{235}$U, and $^{232}$Th are present day concentrations of the respective isotope. In most minerals, $^4$He contribution from $^{147}$Sm is negligible, and therefore omitted from the ingrowth equation; however, it is considered for some REE-rich phosphates such as apatite grains (Farley and Stockli 2002)

For minerals such as zircon that exclude Sm decay, the apparent age can then be calculated using the equation:

$$^4He = 8\ {}^{238}U(e^{\lambda_{238}t} - 1) + 7\frac{^{238}U}{137.88}\left(e^{\lambda_{235}t} - 1\right) + 6\ {}^{232}Th\left(e^{\lambda_{232}t} - 1\right) \qquad \text{Equation 2}$$

where the factor 137.88 in equation 2 is the $^{238}$U/$^{235}$U ratio of natural uranium (Farley and Stockli 2002). This expression assumes (1) secular equilibrium, (i.e. when isotope content is constant because decay rate is equal to production rate) and (2) an initial He concentration of zero, which is a generally a safe assumption because atmospheric He is very low (Farley 2002).

Diffusivity of He determines closure temperature of a mineral so its understanding is integral to the dating process. Diffusivity is investigated in laboratory experiments which quantify the He behaviour but there are limitations to these studies since they are carried out at temperatures higher than in nature, and therefore low temperature data must be extrapolated (Ehlers and Farley 2003). $^4$He loss is thermally-activated and therefore a linear Arrhenius plot confirms the temperature dependency of diffusion (Farley 2002). However, radiation damage in zircons can yield erratic Arrhenius plots (Farley 2002).

### 3.2.3 Partial Retention Zone

The partial retention zone (PRZ) is the temperature or depth range within which $^4$He is partially retained within the crystal lattice because of thermally activated diffusion (Figure 12, Reiners and Brandon 2006). At sufficiently high temperatures and depths, $^4$He products diffuse outside

of the crystal lattice and are lost because of the high diffusivity and at the lower limit of the PRZ, $^4$He remains trapped in the grain. Rapidly cooled samples pass through the PRZ, lose little $^4$He during cooling whereas samples that spend significant time in the PRZ continually lose $^4$He. The slower the cooling rate, the greater the sensitivity of (U-Th)/He age to subtle factors such as grain size and zonation (Ehlers and Farley 2002).

In apatite, the PRZ has a temperature range of ~ 40-80 ˚C and its closure temperature is ~ 68 ± 5 ˚C (Farley 2002). In zircon, the PRZ is ~ 130-200 ˚C with a closure temperature of ~ 185 ± 10 ˚C (Stockli and Wolfe 2009, Reiners et al. 2002).

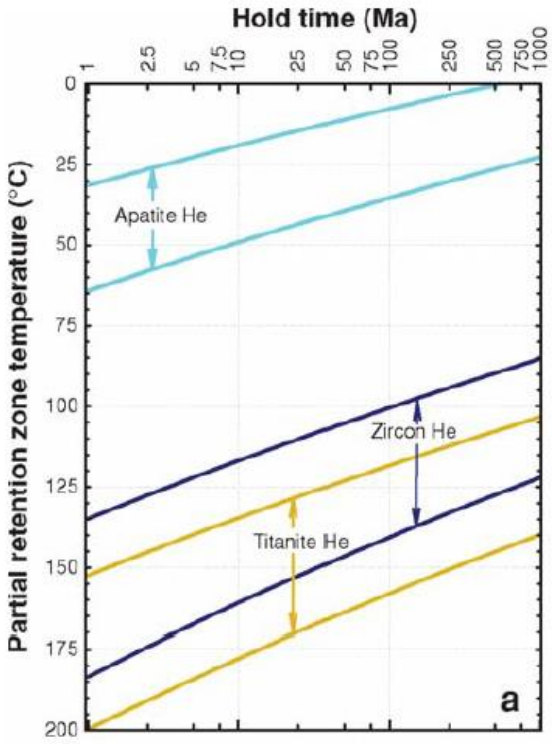


Figure 12: Partial retention zone (PRZ) for apatite, zircon and titanite He thermochronometers wither upper and lower boundaries defined by 90 % and 10 % retention, after being held at a steady temperature for a specified amount of time (Reiners and Brandon 2006).

### 3.2.4 Radiation Damage

Damage, resulting from radioactive decay can result in alteration of the crystal lattice. Wolfe and Stockli (2010) report that radiation damage in apatite causes a trapping affect that block

pathways for He to diffuse. In zircon however, He diffusion is strongly affected by high degrees of radiation damage (Reiners 2005). In step-heating experiments by Guenthner (2013), diffusion rates increase by up to 10 orders of magnitude in heavily damaged (~8 x $10^{18}$ α /g) samples, which was attributed to increasingly interconnected pathways allowing for fast transport. Consequently, the damaged sample has a lower closure temperature (Guenthner 2013, Farley 2002).

### 3.2.5 α-ejection and correction

α decay is an energetic process and results in the α-recoil of the parent nucleus and emission of a $^{4}$He. The distance that the α particle is displaced is referred to as the stopping distance, which varies depending on the decay series and the density of its host (Farley and Stockli 2002). Stopping distance in apatite is ~19.3 μm for the $^{238}$U-series, ~22.4 μm for $^{235}$U-series, and 22.2 μm for the Th-series (Farley and Stockli 2002). Stopping distances are important since decay near the grain boundary can result in a α particles ejected outside of the grain, leading to an underestimate of the age since the grain would have an inaccurately low proportion of daughter products (Farley and Stockli 2002). α implantation is less likely to happen, because apatite and zircon usually have much higher concentrations of U and Th relative to surrounding mineral grains (Farley and Stockli 2002). α corrections are made using the measured grain geometry and assume that all crystal surfaces were intact and that the parent nuclide is homogeneously distributed throughout the grain (Farley and Stockli 2002).

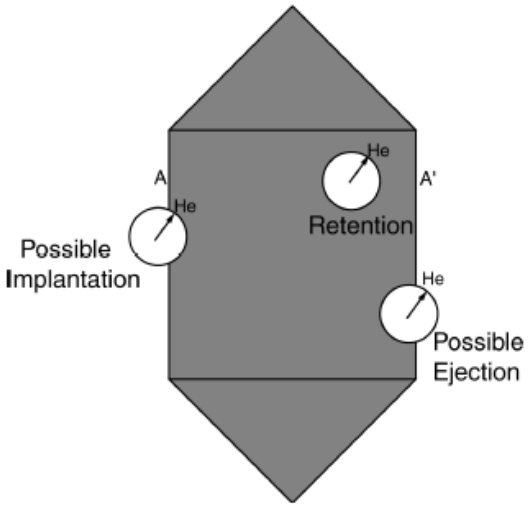


Figure 13: potential trajectories of $^{4}He$ in its host: retention if it is within ~20µm of the grain boundary, possible ejection if it is near the grain boundary, or possible implantation from neighbouring grains (Farley 2002).

The α correction '$F_T$' is the factor by which the measured age must be divided to obtain the α-corrected age and is most strongly influenced by the surface area to volume ratio of the dated crystal and the stopping distance (Farley 2002). Figure 14 illustrates the decrease in the fraction of $^{4}He$ retained when the crystal diameter drops below ~70 µm, the magnitude of the correction increases rapidly with decreasing grain size. $F_T$ values for $^{238}U$ are higher than $^{232}Th$ because $^{232}Th$ has a higher emission energy resulting longer stopping distances and a greater number of ejections. It is for this reason that grains chosen for dating must be > 70 µm in dimension. Without correction, error from ejection can be up to 10s of % of the calculated cooling age (Ehlers and Farley 2003).

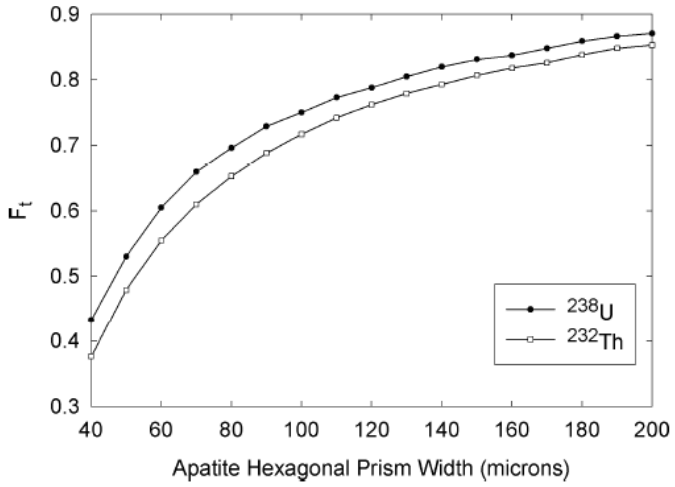


Figure 14: effects of α ejection on a hexagonal apatite crystal where $F_T$ is the total fraction of α retained (Farley 2002).

### 3.2.6 Source of error

He diffusion occurs at grain boundaries, therefore the outermost portion of the crystal will have lower He concentration than in the interior (Farley 2002). Since diffusion rate is dependent on He concentration gradient, a depleted rim will result in a slowed He loss rate and yield a slightly higher closure temperature (Ehlers and Farley 2003). Conversely, a zoned grain where the boundary has a higher concentration of U and Th, there will be an elevated He loss rate and result in an age that is too young (Ehlers and Farley 2003). When a gain is zoned, it is almost always the case that all grains in the sample are zoned resulting in a consistently young age (Ehlers and Farley 2003).

## 3.3 Sampling strategy

The initial sampling strategy for this project was a linear transect along Highway 8 on mainland Nova Scotia. Highway 8 runs approximately NW-SE, which is roughly perpendicular to the margin and the rift-related extensional structures. Sample locations were selected based on 1:10 000 regional geological maps of Nova Scotia and corresponding potential outcrop locations as determined by Google Earth. Out of 18 potential outcrops that we identified along Highway 8, only six were sampled because of poor road accessibility, forest fires (which bias our results), or natural overgrowth. About 60% of the marked outcrops on the Nova Scotia Geologic Map visited along the highway consisted of granitoid boulders that were not sampled because it could not be determined whether they were in place. From the six samples initially collected (CC01 to CC06), CC04 was not further studied because the very fine grain size of this meta-sediment. To supplement the number of data point, sample CC07 was collected at Crystal Crescent Beach because it was accessible, but not along the transect. Samples CC01, CC02, CC03, CC05, and CC06 are located on this transect.

## 3.4 Sample location and petrology

Sample locations are illustrated in Figure 5 with the elevation profile and sample locations on the transect generated by Google Earth in Figure 15. None of the sample exceeds 150 m elevation and lithologies consist of SMB granitoids and Meguma Group metasediments. Sample locations, lithology, and thermochronometers used are summarized in Table 1.

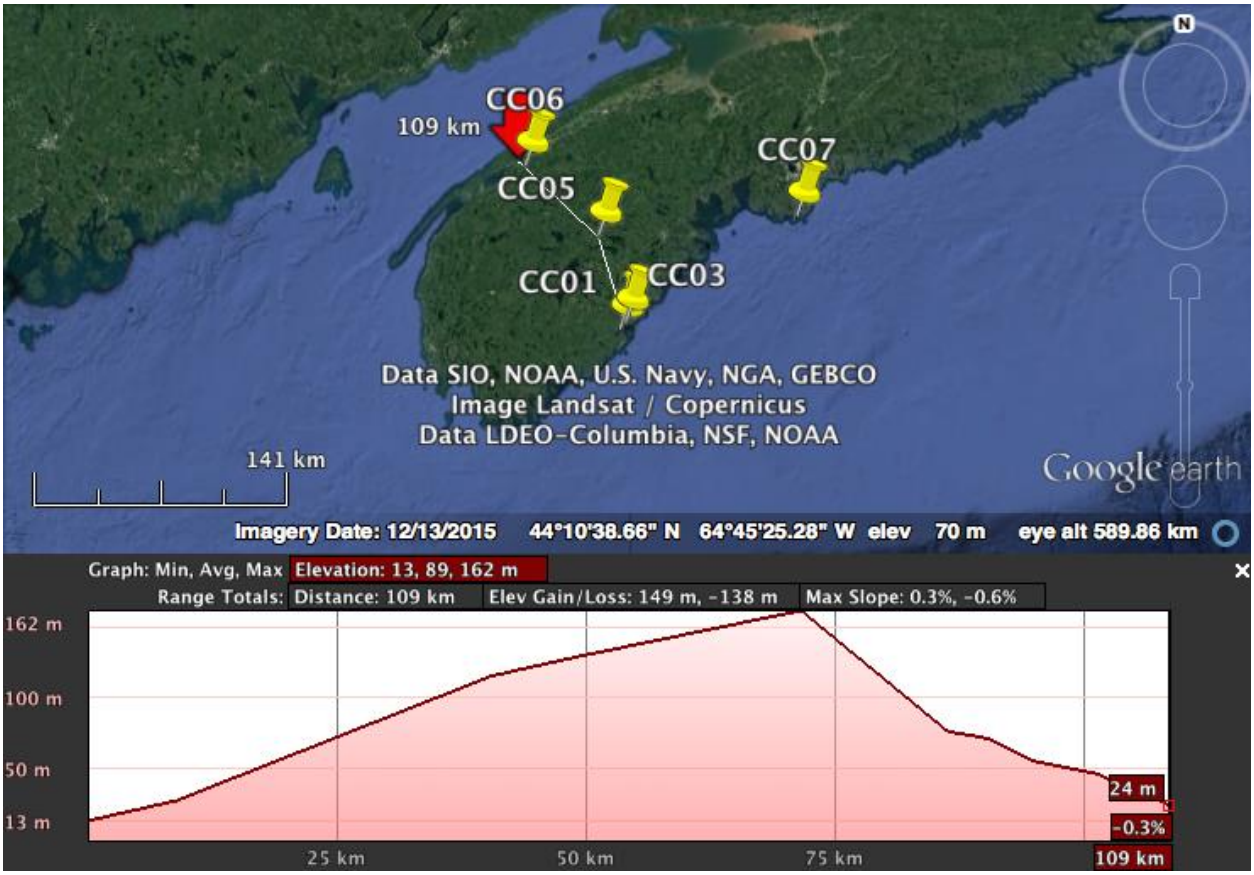


Figure 15: Elevation profile of sampling transect across mainland Nova Scotia (Google Earth 2017).

Table 1: Sample list, location, lithology and thermochronological analyses processed. Abbreviations are: bt, biotite; AHe, apatite (U-Th)/He; ZHe, zircon (U-Th)/He.

| Sample | Location | Latitude | Longitude | lithology | AHe | ZHe |
|---|---|---|---|---|---|---|
| CC01 | Port Mouton | 43˚ 54.262 | 64˚ 48.523 | quartz syenite | x | x |
| CC02 | Port Mouton | 43˚ 54.171 | 64˚ 48.516 | bt-quartz syenite | | |
| CC03 | Port Mouton | 43˚ 54.171 | 64˚ 48.516 | bt-psammite | x | x |
| CC05 | South Brockfield | 44˚ 22.361 | 64˚ 58.354 | meta-siltstone | | x |
| CC06 | Harvest Rd at Highway | 44˚ 42.122 | 65˚ 29.180 | porphyritic bt- | | x |
| CC07 | Crystal Crescent Beach | 44˚ 26.945 | 63˚ 37.214 | monzogranite | | x |

## 3.5 Sample preparation

### 3.5.1 Crushing, electric pulse disaggregation and sieving

About four-five kg of CC07 was processed through the jaw crusher (Figure 16a) and disk mill (Figure 16b) at Dalhousie's Rock Disaggregation Facility. The jaw crusher breaks down large samples into gravel-sized particles that can then be processed in the disk mill. The disk mill consists of two rotating plates whose distance can be set to the desired coarseness of the sample. The sample must be processed gradually in decreasing grain size otherwise the chute becomes obstructed. Three runs were completed for CC07 at 1cm, 0.5 cm, and 0.1 cm.

Samples CC01, CC02, CC03, CC05, and CC06 were sent to Overburden Drilling Management in Ottawa for electric pulse disaggregation (EPD) using a Spark 2. The Spark 2 Electric Pulse Disaggregator employs high frequency pulses that fracture grains along weak zones such as grain boundaries, ideally leaving a greater proportion of preserved grains than traditional crushing methods.

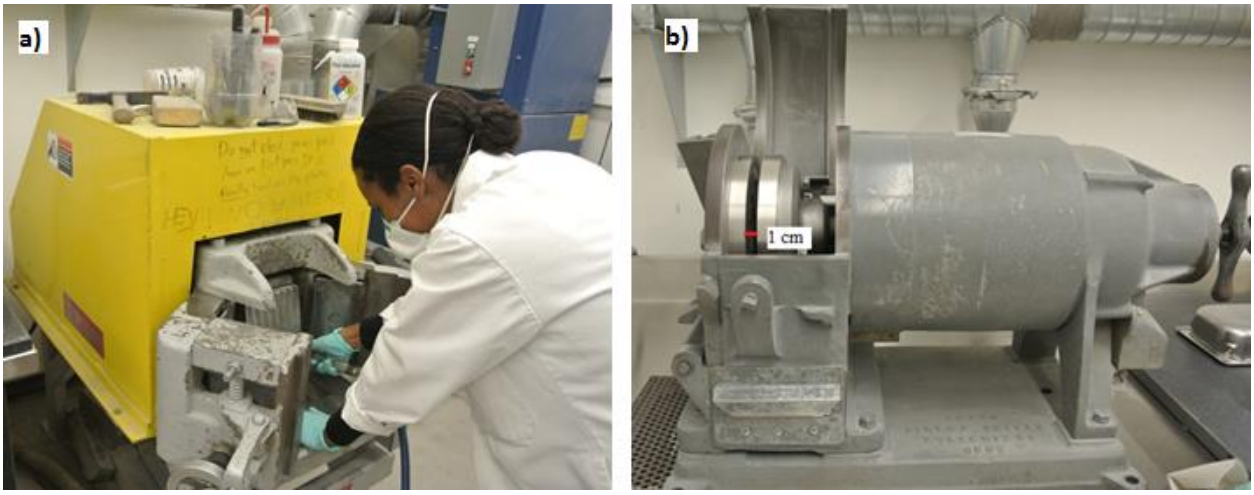


Figure 16: Bertha Louis demonstrating how to clean and operate the jaw crusher. (b) The disk mill set to a 1 cm gap for the first of 3 runs.

The crushed samples were manually sieved (Figure 17) to separate grains < 250 µm, which were then processed through a Wifley water table.

### 3.5.2 Water table processing

Water table processing was completed using a Wilfley Table, which serves to separate the < 250 µm based on the mineral density. This process segregates low density minerals such as clays and micas, medium-density minerals such as quartz and feldspars and high density minerals such as oxides, garnet, pyroxene, apatite and zircon. The sieved sample is put through vibrating feeders, mixed with water and passes over the ridges of the table as the table, driven by a piston engine, shakes back and forth while flooded by a steady water flux. The densest portion passes through the tube on the far side of the feed while becoming progressively finer toward the feed and collects in 7 spigots (Figure 18). All fractions are decanted and dried in an air-forced Memmert oven at 50 ˚C, but only sample from the first three spigots continue for further processing.

Figure 17: Sample CC07 being sieved after three runs in the disk mill.

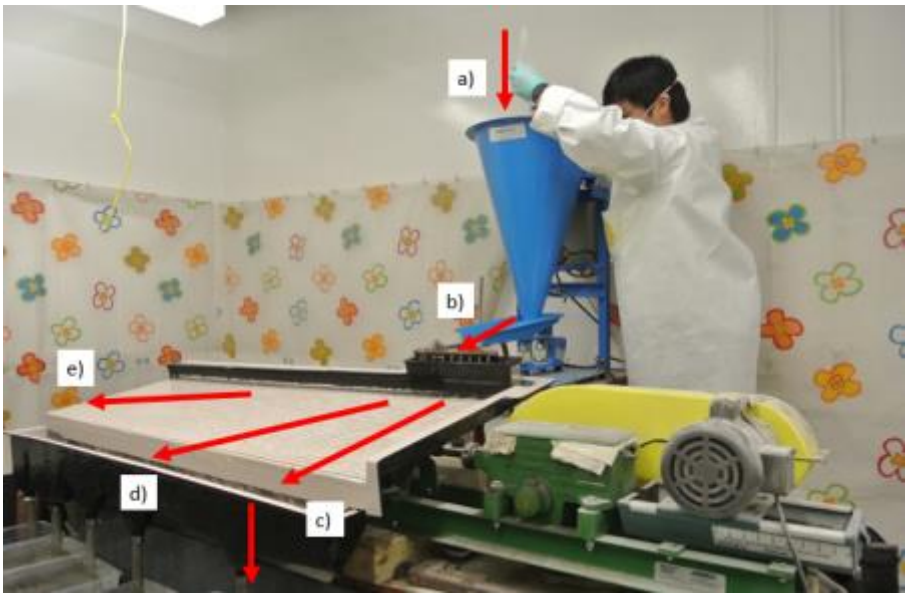


Figure 18: Water table processing using a Wilfley Table: a) sample enters the vibrating cone and collects at the vibrating base (blue) and b) moves through the feed where it then mixes with running water where the sample separates into a gradient of densities, c) the fine and light fraction is entrained in the running water and floats over the table's ridges, moves through the spigot and collects in the first bin, d) the slightly denser fraction collects at the next spigot, e) the densest fraction moves along the ridges to the opposite end of the Wilfley Table.

### 3.5.3 Heavy liquid mineral separation

Heavy liquid separation is completed using Lithium Metatungstate (LMT) a salt highly soluble in water, which allow obtaining high-density solutions of up to 2.95 g/cm$^3$ at room temperature. The purpose of this step is to separate grains based on their density relative to LMT. Density of apatite and zircon are ~3.17 g/cm$^3$ and ~4.65 g/cm$^3$, respectively, meaning that once mixed with the LMT, they will sink at the bottom of the funnel while lower density material (such as quartz and feldspar crystals for example) floats to the surface (Figure 19a). Before heavy liquid separation, strongly magnetic minerals were removed using a hand magnet to minimize the sample quantity and prevent LMT staining from these iron oxides. Once the sample is immersed and thoroughly mixed with the LMT, it is left for 30 minutes to settle before heavy fraction retrieval. This process is repeated until few grains settle (~3 times per sample). The final product is thoroughly rinsed and dried at 50 ˚C, and consist of material >2.85 g/cm$^3$.

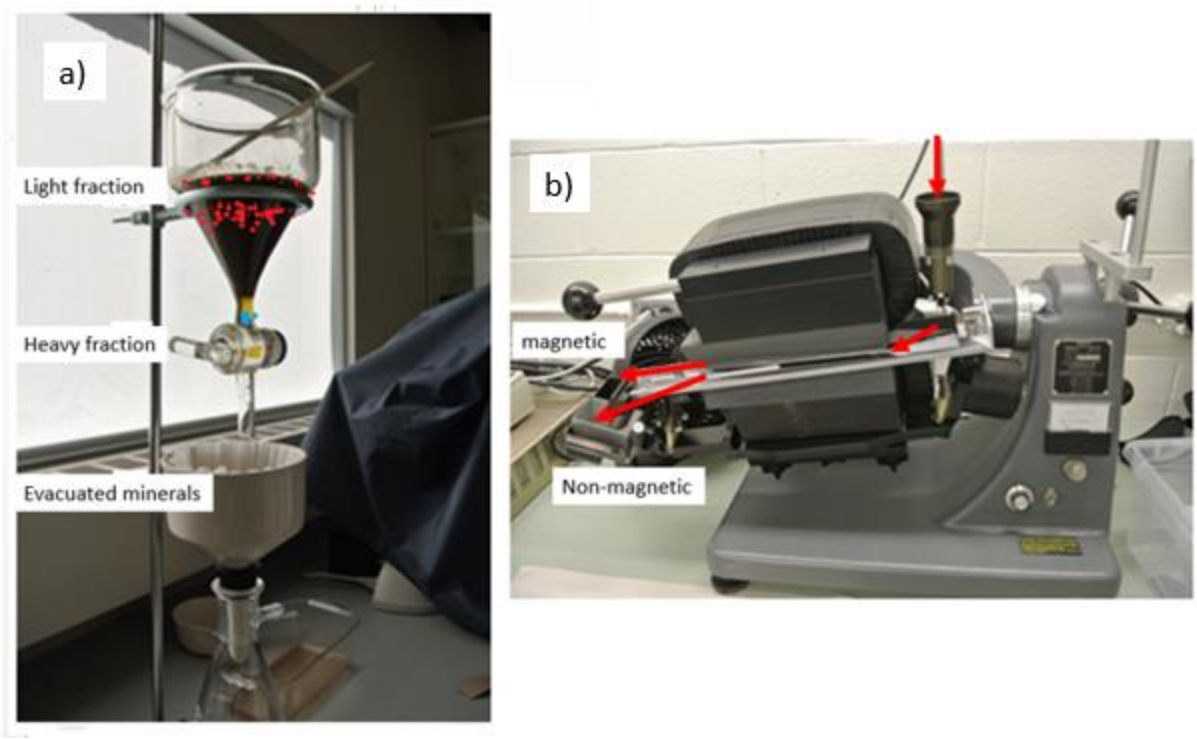


Figure 19: a) LMT heavy liquid separation set-up where the light fraction floats to the top, annotated in red, and the heavy mineral fraction settles at the bottom before retrieval and filtration, annotated in blue. b) Frantz magnetic separator annotated to illustrate where sample is introduced (vibrating feeder) and moves down the tilted rail. The part in black is the magnet generating a magnetic field of desired intensity (up to 1.2 A in this study). The sand travels through this field and the nonmagnetic sand fraction unaffected by the induced magnetic field moves along the steepest slope gradient while the magnetic grains are collected at an adjacent container.

### 3.5.4 Frantz magnetic separation

Apatite and zircon are non-magnetic minerals, therefore by removing all magnetic material the fraction is purified. The sample slowly passes through the vibrating feed and lands on a vibrating plate both tilted along its long- and short-axis. Without a magnetic field, all of the sample would end up in the non-magnetic chute since the short axis is tilted toward it. When the magnet generates a magnetic field, its force on the magnetic fraction is greater than the gravitation force from the short axis tilt and ends up in the opposite chute (Figure 19b). Each sample is run through the Frantz three times at increasing currents: 0.4 A, 0.8 A, and 1.2 A.

## 3.6 Apatite and zircon (U-Th)/He dating procedure

### 3.6.1 Apatite and zircon grains picking

Picking datable grains is performed using a SMZ1500 Nikon stereoscopic microscope attached to a camera driven by NIS Elements software. Grains are identified and selected under reflected, transmitted and polarized lights. Ideal grains are euhedral, inclusion-free, and 70-150 μm in size. Inclusions can be problematic particularly for apatite crystals, because the presence of zircon inclusions could significantly bias the He content measured during degassing and would yield a cooling age older than the actual age. If grains under cross-polarized light do not evenly go into extinction, it is likely that the grain has inclusions and will not produce an accurate age.

A euhedral apatite is a tetragonal prism with high relief and birefringence, and has white-yellow-brown-blue pleochroism. The absence of datable apatite crystals in the samples resulted in the decision to process zircons using (U-Th)/He dating. To increase the efficiency of the picking process, the heavy fraction was passed through a second heavy liquid separation using Methylene Iodide (MI), another heavy liquid with a density ~3.3 g/cm$^3$. Zircon, with a density of ~4.65 g/cm$^3$ settles out of MI. Zircons are octagonal prisms with characteristic pink/green birefringence that apatite does not have.

### 3.6.2 Measuring and packing grains for He-degassing

Before packing the grains for degassing, each grain is photographed and measurements are taken for $F_T$ calculation. Apatite (Appendix B1 – B10) and zircon (Appendix B11 – B25) grain photos with long- and short- axes lengths are also useful for anaylsis since it can be used to help explain data anomalies if there are fractures or inclusions.

Under the stereoscopic microscope, each grain is individually placed and crimped in a platinum capsule kept in place with parafilm. Packing was completed by Roman Kislitsyn from Dalhousie's Noble Gas Laboratory.

For AHe, five euhedral, inclusion-free grains between 70-150 µm were picked from samples CC01 and CC03. For ZHe, only 3 aliquots were dated because of the higher analytical cost. Analytical procedures for (U-Th)/He dating involves two main steps: measurement of He content and of U, Th, and Sm content.

### 3.7.3 He-degassing

$^{4}$He was degassed by laser heating in an ultra-high vacuum (UHV) cell at Dalhousie University's Noble Gas Lab. Isotopic dilution with a $^{3}$He spike was used to improve resolution of the spectrometer. $^{3}$He and $^{4}$He are measured in two solutions: (1) standard solution and a spike, and (2) the unknown sample and a spike. He measurements capture the $^{3}$He/$^{4}$He ratio of the unknown sample and by using this ratio and the $^{3}$He concentration of the spike, the grain content in $^{4}$He can be calculated. To accomplish this, a laser heats the sample to temperatures > 1000 ˚C, degassing the grain and moving the gasses in a vacuum maintained at 1.3 x $10^{-9}$ T. The gases then move into a cryotrap at 18 ˚K where they all freeze and the temperature then increases to 37 ˚K at which point only H and He are mobilized. The H and He are then ionized and measured in a quadrupole mass spectrometer. Once He content is calculated, grains were dissolved for obtaining U, Th ± Sm content at Colorado Trail laboratory.

### 3.7.4 U-Th-Sm content

For my samples, parent isotope extraction took place at the Colorado Trail laboratory (Boulder). Apatite grains are dissolved in a solution of $HNO_3$ including a $^{235}$U, $^{230}$Th, and $^{149}$Sm spike and heated at 80 ˚C for 1-2 hours. Zircon grains are dissolved in HF and $HNO_3$ (~20:1 ratio) and at heated at 200 ˚C for four days in a heavy metal bomb. Once dry, HCl is added and left at 200 ˚C for 12 hours, then mixed with $HNO_3$ and heated to 80 ˚C. Zircon can be dissolved exclusively with HF but cannot be run in the ICP-MS unless it is in a $HNO_3$ solution.

Once dissolved with $HNO_3$, U, Th, and Sm are measured with a Thermo Element 2 ICP-MS. Liquid sample is drawn through an autosampler and enters a nebulizer that turns the sample into an aerosol. The aerosol is then heated in plasma until molecules are excited to a

state of ionization.  At this point, ions are accelerated in an electric field and then pass through a magnetic field that bends the particle path depending on its mass/charge ratio and hits a detector that then counts the number of ions of each type.

## Chapter 4: (U-Th)/He Results

From the six bedrock samples separated, 33 % yielded datable apatite crystals and 83 % yielded datable zircons. It is difficult to predict datable grain yield in samples due to the stringent criteria required for (U-Th)/He thermochronology. Some samples simply did not contain apatite or zircon, while in others, they were ubiquitous but did not fulfill the quality criteria.

This chapter first describes (U-Th)/He results, provides explanations for anomalous ages and isotope content. AHe, ZHe, and AFT from this study and compiled from the literature are used to extract cooling rates which are converted into exhumation rates and compared to deduce regional variation in Nova Scotia.

### 4.1 Apatite (U-Th-Sm)/He age results

AHe cooling ages were obtained from two samples using five aliquots each. Instrumentation used for daughter and parent isotope analysis are considered calibrated since the Durango apatite standard yielded an age of 30.5 ± 1.83 Ma (± analytical error associated with isotope analysis in Ma) and has an actual age of 32.1 Ma (Farley 2000). $F_T$ of the apatite standard is 1 because the grain is taken from a larger apatite crystal and not within the stopping distance to the crystal boundary. Single aliquot ages are reported with their analytical error and the mean ages for each sample are reported with a mean error calculated using the equation:

$$Error = \frac{STD\ (A_1, A_2, \ldots, A_n)}{\sqrt{n}} \qquad \textit{Equation 3}$$

Where numerator is the standard deviation of all aliquots and the denominator is the square root of the number of aliquots.

#### 4.1.1 Sample CC01

The mean corrected ages of the five aliquots is 193 ± 28Ma (CC01). Aliquot CC01-2 (303.2 Ma) is over 100 Ma older than the four other aliquots, which range from 150.6 – 182.3 Ma (Table 2). The corrected versus raw age range is similar and CC01-2 remains an outlier, ~90 Ma older than

the other four aliquots. Further, CC01-2 yielded anomalously low U concentration compared to the four other aliquots (Table 2) and could be a result of improper dissolution or fracturing during degassing and fragments lost in the capsule that would lead to unaccounted daughter products and a comparatively older age. Radiation damage could also cause an older age because it decreases He diffusivity. Upon inspection of the grain photo in Appendix B2, it is possible that an inclusion is present, and if it is zircon, which does not dissolve in the apatite dissolution procedure, it would provide unaccounted daughters since it would contribute $^{4}He$ during degassing, but none of its parent isotopes resulting in an older age. If we consider CC01-2 an outlier and exclude it, the mean age becomes 165.4 ± 7.0 Ma.

### 4.1.2 Sample CC03

For sample CC03, five aliquots yielded a mean corrected age 242.2 ± 32.0 Ma (Table 2). Aliquot CC03-2 (365.3 Ma) is over 120 Ma older than the four other aliquots, which range between 195.4 and 244.1 Ma, and if excluded, the mean age becomes 211.4 ± 11.2 Ma. Raw ages exhibit a similar trend where CC03-2 ~60 Ma older than the other aliquots. The reason for yielding an older age could be the same as CC01-2 where the grain is fractured during degassing and pieces are left behind, radiation damage, not fully dissolved for parent isotope analysis, or has zircon inclusions. Parent and daughter isotope concentrations do not seem anomalous compared to other grains.

## 4.2 Zircon (U-Th)/He age results

Five ZHe ages were obtained using three aliquots each. Based on the age yield of the standard of 27.2 ± 1.6 Ma from Fish Canyon Tuff with an actual ZHe age of 28.2 Ma, the instruments used for isotopic analysis are considered calibrated. Unlike the apatite standard, the zircon standard used is not from a large crystal so there is a $F_T$ correction value of 0.82. Errors discussed each aliquot are analytical error unless otherwise stated. Three aliquots were used compared to the five for AHe because of the limited datable zircon grains and the greater cost of ZHe compared to AHe. Consequently, this makes determining outliers a difficult task.

### 4.2.1 Sample CC01

The three zircon aliquots have a large range from 140.3 – 280.4 Ma and yield a mean age 212.1 ± 40.5 Ma. Uncorrected ages also show a large range from 119 - 208 Ma. CC01-2 is twice the age of CC01-1 and has approximately half of the Ue value (Table 3) meaning the parent isotope concentration is comparatively low possibly resulting from fragments breaking off during laser heating for He degassing. CC01-3 has a length to width ratio of ~3.5:1 (Appendix B3) which is higher than ideal because the greater surface area to volume ratio makes the grain more susceptible to ejection or implantation.

Table 2*:* Reduced data from apatite (U-Th)/He dating.

| Sample | Corrected age (Ma) | Analytical error (Ma) | U (ppm) | Th (ppm) | $^{147}$Sm (ppm) | Th/U | [U]e | He (fmol) | $F_T$ | Raw Age (Ma) |
|---|---|---|---|---|---|---|---|---|---|---|
| aDUR-46 | 30.5 | 1.83 | 1.9 | 37.8 | 2.3 | 19.43 | 10.6 | 89.9 | 1.00 | 30.50 |
| aCC01-1 | 158.2 | 9.49 | 14.5 | 2.0 | 13.6 | 0.14 | 15.1 | 22.5 | 0.69 | 109.46 |
| aCC01-2 | 303.2 | 18.19 | 0.5 | 1.1 | 4.5 | 2.15 | 0.8 | 4.4 | 0.73 | 222.46 |
| aCC01-3 | 150.6 | 9.04 | 5.6 | 0.6 | 1.6 | 0.10 | 5.7 | 20.3 | 0.76 | 115.12 |
| aCC01-4 | 182.3 | 10.94 | 3.6 | 2.2 | 21.9 | 0.61 | 4.3 | 14.9 | 0.74 | 135.71 |
| aCC01-5 | 170.6 | 10.24 | 14.2 | 4.2 | 11.3 | 0.30 | 15.2 | 17.4 | 0.66 | 111.99 |
| aCC03-1 | 244.1 | 14.65 | 67.2 | 13.3 | 20.9 | 0.20 | 70.4 | 294.2 | 0.74 | 181.31 |
| aCC03-2 | 365.3 | 21.92 | 51.8 | 15.7 | 29.5 | 0.30 | 55.5 | 123.2 | 0.65 | 239.20 |
| aCC03-3 | 207.6 | 12.46 | 46.7 | 2.6 | 19.3 | 0.06 | 47.4 | 125.3 | 0.73 | 150.58 |
| aCC03-4 | 198.5 | 11.91 | 14.0 | 1.0 | 14.2 | 0.07 | 14.3 | 22.9 | 0.69 | 136.99 |
| aCC03-5 | 195.4 | 11.73 | 24.1 | 1.6 | 15.3 | 0.07 | 24.6 | 48.4 | 0.71 | 138.49 |

U, Th, and Sm concentrations in parts per million (ppm); Th/U is the ratio between the two parent isotopes ; [U]e (effective uranium content) is the quantity of U required to produce the amount of $^{4}$He present in the sample if uranium was the sole parent isotope. Ue provides a proxy for alpha production rate as well as for relative radiation damage (Guenthner et al. 2013); He is the quantity measured in femtomols (fmol) equal to $10^{-15}$ mol. $F_T$ is the α-ejection correction that the raw age is divided by in order to attain the corrected age. $F_T$ value depends on the grain shape and is most strongly affected by the surface area to volume ratio. The last column is raw age in Ma, calculated with parent and daughter concentration without $F_T$ correction.

### 4.2.2 Sample CC03

Three zircon range from 215.6 - 184.2 Ma and yield a mean age of 193.6 ± 5.3 M. The range of ages is relatively narrow compared to the other samples and ages are within the analytical

error. Raw ages for the three aliquots are within a 5 Ma range. The precision may be related to the euhedral nature of the grains dated (Appendix B14-16).

The mean ZHe age of CC03 193.6 ± 5.3 is younger than mean AHe age 211.4 ± 11.2 which is problematic since the closure temperature of apatite is lower than that of zircon. This could either be the result of an apatite age that is too old or a zircon age that is too young. An old apatite age could result from fracturing during laser heating for He extraction and loss of fragments which are then not included in the parent isotope analysis and/or implantation of $^{4}$He from neighbouring grains. A zircon age that is too young could be produced by radiation damage where He diffusivity increases because damaged zones form interconnected pathways for $^{4}$He to travel. How close are these mean ages after recalculation of the errors? If they are identical within errors, then this can also mean that there has been a fast cooling episode between 193 and 211 Ma during which the sample has cooled very quickly from both closure temperatures.

### 4.2.3 Sample CC05

Three aliquots of CC05 were dated but the CC01 aliquot resulted in a lost grain, and the mean of the two remaining aliquots is 191.7 ± 21.7 Ma. Raw ages show a similar range 120.26 - 141.25 Ma. Mineral separates from CC05 were very altered and grains were very fine. CC05-1 had a width of < 60 µm, which is to be avoided because of difficulty in handling, possibility of losing the grain, and difficulty performing corrections. CC05-3 width is also < 60 µm therefore may lack age accuracy.

### 4.2.4 Sample CC06

Three aliquots of CC06 were dated and range from 277.1-302.1 Ma, the mean age of which is 290.3 ± 7.2. Raw age ranges from 205.26-235.70 Ma, showing an identical ~30 Ma range to the corrected age. The narrow range shows good reproducibility in age.

### 4.2.5 Sample CC07

Three aliquots of CC07 were dated ranging from 186.0-235.7 Ma, averaging 211.9 ± 14.4 Ma. This is a relatively reproducible data set and corresponds to three euhedral zircon grains. CC07-2 has a U concentration over four times higher than the two other aliquots and also has the youngest age, indicating that it may have experienced radiation damage to the point where He pathways form and diffusivity increases, causing a younger age. A summary of AHe and ZHe ages is provided in Table 4.

Table 3: Reduced data from zircon (U-Th)/He dating.

| Sample | Corrected age, (Ma) | Analytical error (Ma) | U (ppm) | Th (ppm) | $^{147}$Sm (ppm) | Th/U | [U]e | He (fmol) | $F_T$ | Raw Age (Ma) |
|---|---|---|---|---|---|---|---|---|---|---|
| zFCT-15 | 27.2 | 1.63 | 303.9 | 210.4 | 0.0 | 0.69 | 352.4 | 654.9 | 0.82 | 22.43 |
| zCC01-1 | 140.3 | 8.42 | 620.0 | 120.7 | 9.8 | 0.19 | 647.8 | 8764.0 | 0.85 | 118.81 |
| zCC01-2 | 280.4 | 16.83 | 316.2 | 74.2 | 0.5 | 0.23 | 333.3 | 1498.3 | 0.74 | 208.16 |
| zCC01-3 | 215.6 | 12.93 | 812.4 | 233.1 | 17.9 | 0.29 | 866.2 | 5263.0 | 0.76 | 164.63 |
| zCC03-1 | 202.6 | 12.16 | 164.1 | 155.4 | 0.0 | 0.95 | 199.9 | 667.0 | 0.74 | 149.97 |
| zCC03-2 | 184.2 | 11.05 | 624.8 | 125.3 | 28.2 | 0.20 | 653.8 | 3597.1 | 0.78 | 143.69 |
| zCC03-3 | 194.0 | 11.64 | 368.1 | 91.5 | 0.8 | 0.25 | 389.2 | 2154.9 | 0.77 | 149.39 |
| zCC05-2 | 170.0 | 10.20 | 216.2 | 350.9 | 0.0 | 1.62 | 297.0 | 531.5 | 0.71 | 120.26 |
| zCC05-3 | 213.4 | 12.80 | 193.7 | 285.1 | 0.0 | 1.47 | 259.3 | 404.6 | 0.66 | 141.25 |
| zCC06-1 | 277.1 | 16.63 | 245.1 | 147.9 | 0.0 | 0.60 | 279.2 | 1236.1 | 0.74 | 205.26 |
| zCC06-2 | 291.7 | 17.50 | 194.2 | 42.4 | 0.0 | 0.22 | 204.0 | 1110.4 | 0.75 | 219.99 |
| zCC06-3 | 302.1 | 18.13 | 162.1 | 49.4 | 0.0 | 0.30 | 173.5 | 1524.4 | 0.78 | 235.70 |
| zCC07-1 | 213.9 | 12.83 | 139.0 | 59.6 | 0.0 | 0.43 | 152.7 | 2288.7 | 0.83 | 177.54 |
| zCC07-2 | 186.0 | 11.16 | 690.7 | 133.7 | 0.2 | 0.19 | 721.4 | 3732.2 | 0.77 | 143.33 |
| zCC07-3 | 235.7 | 14.14 | 160.1 | 39.4 | 2.8 | 0.25 | 169.2 | 1342.7 | 0.79 | 186.33 |

Legend same as Table 2

Table 3: Summary of mean (U-Th)/He ages with associated error from equation 3.

| Sample # | AHe mean age (Ma) | σ | ZHe mean age (Ma) | σ |
|---|---|---|---|---|
| CC01 | 165.4 | 7.0 | 212.1 | 40.5 |
| CC03 | 211.4 | 11.2 | 193.6 | 5.3 |
| CC05 | - | - | 191.7 | 21.7 |
| CC06 | - | - | 290.3 | 7.2 |
| CC07 | - | - | 211.9 | 14.4 |

### 4.3 Cooling age distribution and cooling rates

Zircon cooling ages along the eastern shore are younger than the sample near Annapolis Royale south of the Bay of Fundy (Figure 20). Zircon ages along the eastern shore range from 193.6 - 212.1 Ma compared to the Bay of Fundy (CC06) ZHe mean age 290.3 ± 7.3 Ma using three aliquots with a relatively small range: 277.1 - 302.1 Ma. The limited AHe ages from this study make trends difficult to deduce. However, the two AHe ages 165.4 Ma and 211.4 Ma correlate well with existing AHe data from Grist (2004) where average SMB age at Mahone Bay yielded 208.5 ± 16.7 Ma and SMB in Halifax yielded 208.5 ± 16.7 Ma and 204.6 ± 16.4 Ma. Samples CC01 and CC03 have a difference in AHe mean age of 56 Ma and are within five km of each other in Port Mouton, but taking into account the large error of the ZHe CC01 age, they could in reality be more similar in age.

Cooling curves in Figure 20 illustrate the cooling rate using AHe and ZHe data from this study and AHe and AFT data from Grist (2004). Cooling curves constructed using data from Grist (2004) are not from the same locations but are proximal to our sample sites and are grouped to form a more complete dataset. Samples CC01, CC03, and CC07 use AHe and ZHe data from surface samples while CC06 uses ZHe from this study and AFT taken from a drill core in Digby at 60 m depth. ZHe and AHe relationships represent the cooling from ~185 ± 10 – 70 ± 5 ˚C (CC01, CC03, CC07), and plotted against cooling age, cooling rate between those two temperatures can be calculated. Then, cooling from AHe (or the lowest temperature

thermochronometer) to the mean annual surface temperature (7 ˚C in Nova Scotia; Government of Canada) can also be deduced, assuming cooling to surface temperature has occurred at a steady rate. For sample CC06, AFT and ZHe data represent cooling from ~120 ± 10 – 185 ± 10 ˚C. Sample CC05 does not have additional data from another thermochronometers therefore its relationship with surface temperature and zero age is plotted. Errors are calculated by obtaining the highest and lowest values using the associated uncertainties from cooling age. Some uncertainties are very high because the high error from cooling age is propagated into cooling rates. Table 4 outlines cooling rates for each sample and the approximate temperature range it corresponds to.

Sample CC01 yields a cooling rate of 2.5 ± 8 ˚C/Ma from 212.1 ± 40.5 – 165.4 ± 7 Ma and decreases to 0.38 ± 0.03 ˚C/Ma until present. The neighbouring CC03 yields a negative rate -6.5 ± 2.1 ˚C/Ma ~200 Ma which is likely the result of fast exhumation which would produce very similar cooling ages in AHe and ZHe systems. From ~200 Ma to present, the sample cooled at 0.33 ± 0.02 ˚C/Ma. The one rate from CC05 represents an average cooling from 191.7 ± 21.7 Ma to present at 0.97 ± 0.16 ˚C/Ma. CC06 between 290.3 ± 7.2-244 ± 18 cools at 1.4 ± 1.7 ˚C/Ma and slows to 0.49 ± 0.05 ˚C/Ma until present. CC07 uses a proximal SMB AHe age from Grist (2004, sample HA in Figure 20) and produces an anomalously high cooling rate of 34 ± 4 ˚C/Ma between 211.9 ± 14.4 – 208 ± 16.7 Ma because of the similar age and slows to 0.34 ± 0.04 ˚C/Ma until present. The similarity in age could be because the HA age lacks accuracy, as its date is produced from only one aliquot.

Cooling rates using AHe-ZHe data are heterogeneous throughout the study area; however, the a general trend the data is that cooling rates from ~290-165 Ma are at least an order of magnitude higher than ~165 Ma to present (seen in CC01, CC03, CC06, CC07).

### 4.4 Exhumation rate

Because temperature increases with depth at a rate given by the geothermal gradient, temperatures can be converted into depths and exhumation rates can be calculated from the equation:

$$\frac{dz}{dt} = \left( \frac{Tc - Ts}{\frac{dT}{dz}} \right) / t \qquad \textit{Equation 4}$$

where Tc is effective closure temperature of the thermochronologic system, Ts is mean annual surface temperature, dT/dz is the geothermal gradient, and t is time. Ts used is 7 ˚C.

CC01 experiences average exhumation at a rate of 0.16 mm/yr from 212.1 ± 40.5-165.4 ± 7.0 and increased decreased to 0.025 mm/yr from 165.4 ± 7.0 to present. CC03 is interpreted to have exhumed rapidly ~200 Ma (approximate average between AHe and ZHe ages) to produce an anomalous negative rate since the cooling ages are very close. Between ~200 Ma to present, exhumation decreases to 0.02 mm/yr. The rate for CC05 is 0.062 mm/yr and is an average from 191.7 ± 21.7 to present since there is only one age available. CC06 has a rate of 0.09 mm/yr from 290.3 ± 7.2 – 244 ± 14.4 Ma and decreases to an average of 0.052 mm/yr until present. CC07 has an anomalously high rate of 2.3 mm/yr from 211.9 ± 14.4 – 208.5 ± 16.7 Ma and decreases to 0.02 mm/yr until present.

Since exhumation rates are derived from cooling age and a constant geotherm, regional trends are the same as that of cooling rate. In other words, exhumation rates are relatively heterogeneous. However, there is a temporal trend of greater exhumation rate between values calculated using two thermochronometric methods (AHe, ZHe, or AFT) that span ~290-165 Ma compared to those calculated from ~165 - present. We can take away from these calculations that exhumation decreased towards the present time, additionally supported by CC05's rate 62 000 mm/Ma (from 191.7 ± 21.7 Ma to present) which is significantly greater than rates using AHe age or AFT age to present (CC01, CC03, CC06, CC07). Exhumation rates are summarized in Table 4.

Table 4: Summary of cooling rate and exhumation rates for the temperature range corresponding to the thermochronometers used. Depth range is calculated using the average geotherm 15˚C/Km obtained by Grist and Zentilli (2003). * indicates AFT data used, with a temperature range of 185-120 ˚C and 120-0 ˚C in cooling rate and 11.9-7.5 km and 7.5-0 km in exhumation rate.

| | | sample number | | | | |
|---|---|---|---|---|---|---|
| | **approximate range** | **CC01** | **CC03** | **CC05** | **CC06*** | **CC07** |
| **cooling rate (˚C/Ma)** | 70-7 ˚C | 0.38 ± 0.03 | 0.33 ± 0.03 | - | 0.49 ± 0.07 | 0.34 ± 0.04 |
| | 185-70 ˚C | 2.5 ± 8 | -6.5 ± 2.1 | - | 1.4 ± 1.7 | 34 ± 4 |
| | 185-7 ˚C | - | - | 0.97 ± 0.2 | - | - |
| **exhumation rate (mm/yr)** | 0-4.2 km | 0.025 ± 0.002 | 0.020 ± 0.002 | - | 0.052 ± 0.004 | 0.020 ± 0.002 |
| | 4.2-11.9 km | 0.15 ± 0.02 | -0.43 ± 0.06 | - | 0.09 ± 0.01 | 2.3 ± 0.3 |
| | 0-11.9 km | - | - | 0.062 ± 0.003 | - | - |

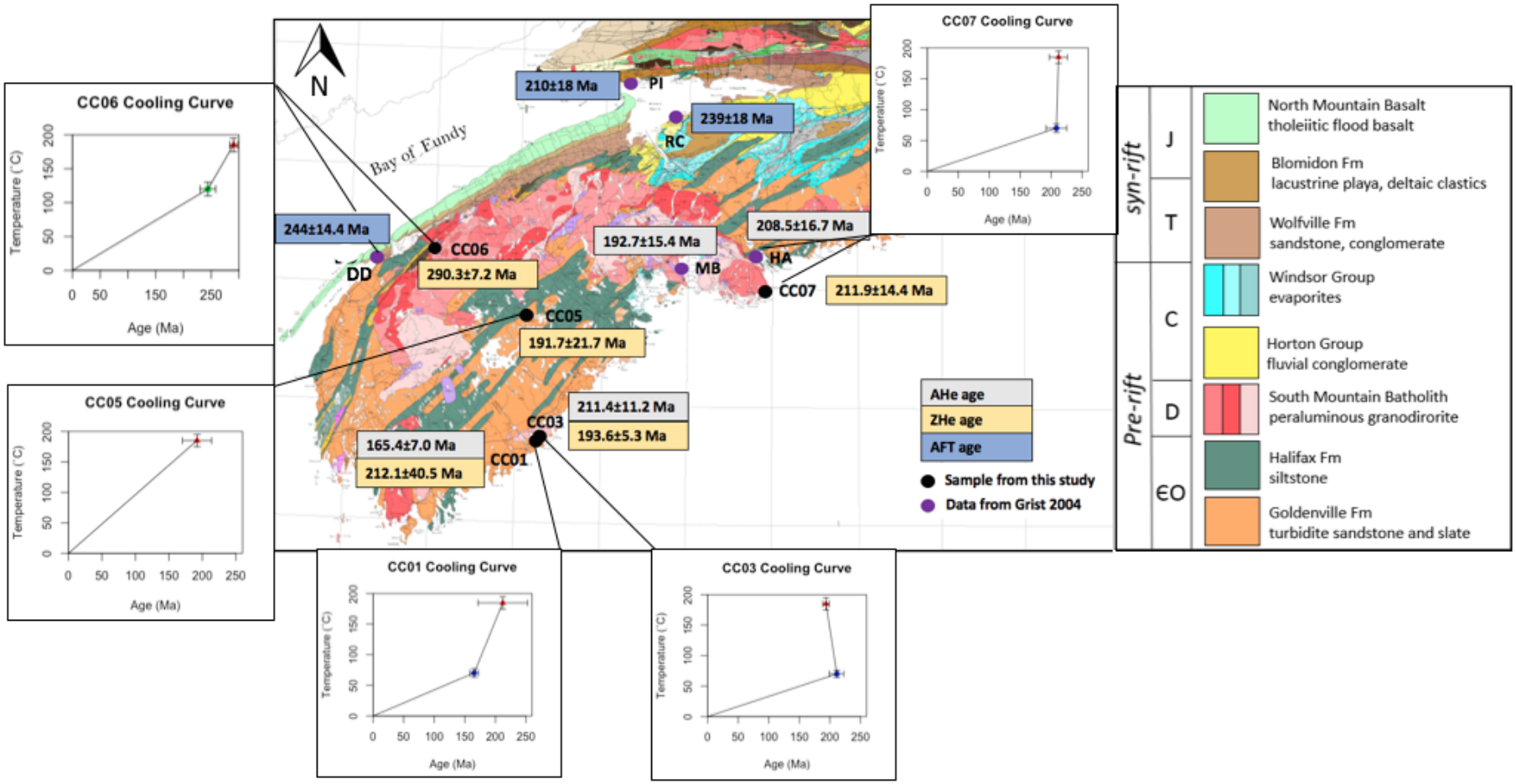


location CC01 and CC03 use AHe and ZHe data from this study in adjacent cooling curves, while CC06 and CC07 use AFT and AHe data (respectively) from Grist (2004). The simplified bedrock geology legend differentiates pre-rift from syn-rift lithologies (White 2012).

# Chapter 5: Discussion

## 5.1 Exhumation on the Scotian passive margin

AHe and ZHe data on mainland Nova Scotia indicate that the low temperature thermal history of the region is dominated by late Triassic to mid Jurassic exhumation. AHe ages along the eastern coast are 165.4 ± 7 Ma and 211.4 ± 40.5 Ma and ZHe ages range from 193.6 ± 5.3 Ma to 290.3 ± 7.2 Ma. During this period, Nova Scotia was in an extensional regime, actively rifting from its Moroccan conjugate. Rifting causes continental crust to thin and asthenosphere upwells, resulting in an elevated geotherm. The uplift and subsequent erosion of a warm, thermally buoyant crust, due to continental rifting is the most likely explanation for (U-Th)/He cooling ages in this study.

Cooling ages of 244 Ma (AFT) and 290 Ma (ZHe) proximal to the 202 Ma North Mountain Basalt near the Bay of Fundy indicate that CAMP magmatism did not affect the cooling ages of these samples.

The significance of the cooling ages from this study is that exhumation since ~165 Ma (youngest AHe age) was less than ~4 km (using a 15 ˚C/km geotherm and 7 ˚C mean surface temperature; Grist and Zentilli 2003) and has been relatively stable. Further, the reported post-rift contraction which occurred in the mid Jurassic does not seem to affect the recorded thermal history. However, this is unsurprising since the low geotherm would require more than the ~1.5 km vertical movements Withjack et al. (1995) estimated. Further, isostatic rebound associated with Quaternary deglaciations is not recorded in mainland Nova Scotia's thermal history. Although the cooling ages do not record any drastic post-Jurassic vertical movements, it is possible that vertical movements did occur but not to the magnitude required to exhume rocks from the depth of the closure temperature (i.e. <5 km as calculated above). Grist and Zentilli (2003) used the lack of long-confined tracks in their AFT analysis that would be required to evidence samples being near surface since cooling past ~120 ˚C to evidence a history that is more dynamic than just gradual peneplanation.

Cooling rates obtained in this study are difficult to interpret considering the few data points and propagation of error, but suggest cooling rates one order of magnitude higher between ~185 - 75 than from ~70 Ma to present (0.38 - 0.48 ˚C/km) which is comparable to rates modelled in the Norumbega Fault System on the US margin (West et al. 2008). Again, this would be consistent with the post-rift thermal relaxation that would occur.

### 5.2 Along-strike variation in exhumation between US and Scotian margins

Low temperature cooling ages on the US margin are younger than in Nova Scotia and show differential exhumation. For example, AHe ages from the Blue Ridge escarpment range from 200 - 120 Ma on the Blue Ridge Upland and 100 - 70 Ma in the inner piedmont (Spotila et al. 2004). The US margin is more strongly influenced by Cretaceous exhumation and shows a younging trend toward the coast (Spotila et al. 2004). Younger ages toward the coast could also be the case on the Scotian Margin, but is not conclusive due to the limited data.

One of the equally evident differences between the two margins is the vastly different geotherm. The geotherm obtained from AFT modelling in New England is ~30 ˚C/km (Roden-Tice 2009) which is significantly hotter than in Nova Scotia (~15 ˚C/km), which could help explain the differences in ages from Scotian to US margin. Assuming a closure temperature of 70 ˚C, 2 km of erosion in the US margin would exhume rocks with a 0 AHe age, however 2 km of erosion in Nova Scotia would not alter the AHe age.

Further, The North American Plate passed over the Great Meteor Hotspot during the Cretaceous and Roden-Tice et al. (2009) suggest that their AFT ages reflect resulting long-lived thermal anomaly that would explain the observed postorogenic extension. Additionally, Menke et al. (2016) propose that the North Appalachian Anomaly (NAA), a 400 km wide low velocity anomaly in southern New England is caused by small scale asthenospheric upwelling separate, but coincidentally proximal to the hotspot track. The preferred process behind the NAA is edge driven convection, which is when a thick stable continental crust juxtaposes thin crust (ie. Laurentian craton and thinned continental crust) and is a source of instability (Menke et al.

2016). Such anomalies are not unique to the northern Appalachians, although it is the most thoroughly studied, and this hypothesis is not unique and able to explain similar anomalies in the central Appalachians, South Carolina, and Louisiana (Menke et al. 2016). If the upwelling causing the NAA is responsible for the low temperature thermal history of surface rocks, there does not seem to be an immediate explanation as to why the NAA terminates where it does and why its effects do not extend to the Scotian margin.

Upon investigation of current studies taking place in the northeastern states, it becomes evident that there are dynamic processes taking place, driving the topography and they seem integrally different from those occurring on the Scotian margin. Mainland Nova Scotia lacks the striking topography and has no rift flank. Amidon et al. (2016) propose that the topography to the south being maintained may be due to sustained isostatic response because of its thick and buoyant crust. In other words, the overprinting of orogens have progressively thickened the crust causing it to be more positively buoyant and therefore the effect of erosion and incision on the overall elevation is low.

Withjack et al. (1995) proposed ridge push as a possible driver for post-rift shortening in the Fundy Basin and noted NW-SE and N-S shortening directions. One hypothesis that is currently being investigated is the effect of ridge-push at the spreading centre when spreading direction changes (Amidon et al. 2016). A cluster of 90 – 75 Ma AHe ages in the White Mountains could be caused by a change in Atlantic stress regime from 84 – 64 Ma, and could be a good explanation for Atlantic-wide late Cretaceous passive margin reactivation (Amidon et al. 2016).

### 5.4 Uncertainty and future studies

Much of the uncertainty from this project is sourced in the spread of ZHe ages since only three aliquots did not allow for us to determine a statistically significant age when there is poor precision. In future studies, using at least four aliquots would allow for more meaningful interpretations. In addition, the wide spread of ages and poor geographic age consistency

could be the result of zoning, therefore measuring zonation in sample grains could help explain the data.

Thermal modelling with new data with existing AHe and AFT using more recent models might produce more accurate thermal histories compared to those completed more than a decade ago.

In future studies, it would be interesting to investigate thermal history across a fault zone much like West et al. (2008) in the Narumbega Fault System. Taking samples across the CCFZ (Figure 4) has not been done and could provide insight into whether there were significant vertical movements during or after rifting.

## Chapter 6: Conclusion

The study of passive margins has, within the last couple decades become a rejuvenated area of study because of its observed non-passive behaviour. Based on this study on the southern mainland of Nova Scotia using apatite and zircon (U-Th)/He anaylsis, we can conclude:

1) AHe and ZHe ages range from 165.4 – 211.4 Ma and 290.3 - 193.6 Ma respectively and most likely correspond to syn- to post-rift erosion during the late Triassic to mid-Jurassic. Cooling rates based on average closure temperature and cooling age yield rates that are one order of magnitude higher from ~ 185 – 70 ˚C compared to ~70 ˚C to surface. This drastic change in rate probably corresponds to the denudational response after rifting and then a relatively low average cooling rate until present. These data do not necessarily rule out vertical movements on the Scotian margin such as those seen in other Atlantic passive margins, however it does require that exhumation since the Triassic to be less than ~ 4 km.

2) Compared to the US margin, Nova Scotia's topographically subdued southern mainland yields much older ages than the dominantly Cretaceous to the south. AHe ages on the Blue Ridge escarpment are 204 – 122 Ma on the upland and 108 – 68 Ma on the piedmont where age decreases towards the coast. Even younger Cretaceous AFT ages of 90 – 75 Ma are found in the White Mountains in New Hampshire and may be a result of small scale asthenospheric upwelling, reactivation of underlying Paleozoic thrust faults, or shifts in seafloor spreading direction.

**References**


Barr, S.M., Raeside, R.P. 1989. Tectono-stratigraphic terranes in Cape Breton Island, Nova Scotia: Implications for the configuration of the northern Appalachian orogeny. Geology, **17**: 822-825.

Chenin, P., Beaumont, C. 2013. Influence of offset weak zones on the development of rift basins: Activation and abandonment during continental extension and breakup. Journal of Geophysical Research: Solid Earth, **118**: 1698-1720.

Dehler, S.A. 2012. Initial rifting and breakup between Nova Scotia and Morocco: insight from new magnetic models. Canadian Journal of Earth Sciences, **49**: 1385-1394.

Donelick, R.A., O'Sullivan, P. B., Ketcham, R. A. 2005. Apatite Fission-Track Analysis. Reviews in Mineralogy & Geochemistry, **58**: 49-94.

Ehlers, T.A., Farley, K.A. 2003. Apatite (U-Th)/He thermochronometry: methods and applications to problems in tectonic and surface processes. Earth and Planetary Science Letters, **206**: 1-14.

Farley, K.A. 2002. (U-Th)/He dating: techniques, calibrations, and applications. Reviews in mineralogy and geochemistry, **47**: 819-844

Farley, K.A., Stockli, D.F. 2002. (U-Th)/He dating of phosphates: apatite, monazite and xenotime. Reviews in Mineralogy and Geochemistry, **48**: 559-577.

Geoffroy, L. 2005. Volcanic Passive Margins. Comptes Rendus Geoscience, **337**:1395-1408.

Grist, A.M. 2004. Aspects of the thermal history of the eastern margin of Canada based on apatite fission track and (U-Th)/He thermochronology. PhD thesis, department of Earth Sciences, Dalhousie University, Halifax, N.S.

Grist, A.M., Zentilli, M. 2003. Post-Paleocene cooling in the southern Canadian Atlantic region: evidence from apatite fission track models. Canadian Journal of Earth Sciences, **40**: 1279-1297.

Guenthner, W.R. 2013. Zircon (U-Th)/He dates from radiation damaged crystals: a new damage-He diffusivity model for the zircon (U-Th)/He thermochronometer. PhD thesis, Department of Geosciences, University of Arizona, Tuscon, Arizona.

Huismans, R.S., Beaumont, C. 2014. Rifted continental margins: The case for depth-dependent extension. Earth and Planetary Science Letters, **407**: 148-162.

Jansa, L.F., Wade, J.A. 1975. Geolgoy of the continental margins off Nova Scotia and Newfoundland. in Offshore geology of eastern Canada, Vol. 2. Regional geology. Edited by W.J. M. Van der Linden and J. A. Wade. Geological Survey of Canada, pp. 51-105.

Hubert, J.F., Mertz, K.A. 1984. Eolian sandstones in the Upper Triassic-Lower Jurassic red beds of the Fundy Basin, Nova Scotia. Journal of Sedimentary Petrology, **54**: 798-810.

Jamieson, R.A., Hard, G.G., Chapman, G.G., Tobey, N.W. 2012. The contact aureole of the South Mountain Batholith in Halifax, Nova Scotia: geology, mineral assemblages, and isograds. Canadian Journal of Earth Science, **49**: 1280-1296.

Keen, C.E., Potter, D.P. 1995. The transition from a volcanic to a nonvolcanic rifted margin off eastern Canada. Tectonics, **14**: 359-371.

Ketcham, R. 2005. Forward and inverse modeling of low-temperature thermochronometry data. Reviews in Mineralogy and Geochemistry, **58**: 275-314.

Kontak, D.J., Archibald, D.A. 2003. (super 40) Ar/ (super 39) age of the Jurassic North Mountain Basalt, southwest Nova Scotia. Atlantic Geology **39**: 47-53.

Lepretre, R., Missenard, Y., Barbarand, J., Gautheron, C. Saddiqi, O., Pinna-Jamme, R. 2015. Postrift history of the eastern central Atlantic passive margin: Insights from the Saharan region of South Morocco. Journal of Geophysical Research: Solid Earth, **120**:4645-4666.

LeTourneau, P.M. 1999. Depositional history and tectonic evolution of late Triassic age rifts of the U.S. Central Atlantic Margin; results of an integrated stratigraphic, structural, and paleomagnetic analysis of the Taylorsville and Richmond basins: Ph.D. dissertation, Columbia University

Louden, K., Wu, Y., Tari, G. 2013. Systematic variations in basement morphology and rifting geometry along the Nova Scotia and Morocco conjugate margin. Divergent Margins, **369**: 267-287.

McKenzie, C.B., Clarke, D. B. 1975. Petrology of the South Mountain Batholith, Nova Scotia. Canadian Journal of Earth Sciences, **12**: 1209-1218.

Melankholina, E.N., Suschevskaya, N.M. 2015. Development of passive volcanic margins of the central Atlantic and initial opening of ocean. Geotectonics, **49**: 75-92.

Menke,W., Skryzalin, P., Levin, V., Harper, T., Darbyshire, F., Dong, T. 2016. The Northern Applachian Anomaly: a modern asthenospheric upwelling. Geophysical Research Letters, **43**: 10,173-10,179.

Nemčok, M. (2016) 'Rifts and Passive MarginsStructural Architecture, Thermal Regimes, and Petroleum Systems', in *Rifts and Passive Margins: Structural Architecture, Thermal Regimes, and Petroleum Systems*. Cambridge: Cambridge University Press.

Pazzaglia, F.J., Brandon, M.T. 1996. Macrogeomorphic evolution of the post-Triassic Appalachian mountains determined by deconvolution of the offshore basin sedimentary record. Basin Research, **8**: 255-278.

Pazzaglia, F.J., Gardner, T.W. 1994. Late Cenozoic flexural deformation of the middle U. S. Atlantic passive margin. Journal of Geophysical Research, **99**: 143-157.

Pazzaglia, F. J., & Gardner, T. W. (2000). Late Cenozoic landscape evolution of the US Atlantic passive margin: insights into a North American Great Escarpment 283-302). Wiley: Chichester.

Poag, C.W., Sevon, W.D. 1989. A record of Appalachian denudation in postrift Mesozoic and Cenozoic sedimentary deposits of the U.S. middle Atlantic continental margin. Geomorphology, **2**:119-157.

Reiners, P.W. 2005. Zircon (U-Th)/He Thermochronometry. Reviews in Mineralogy and Geochemistry, **58**: 151-179.

Reiners, P.W., Brandon, M.T. 2006. Using Thermochronology to Understand Orogenic Erosion. Annual Review of Earth and Planetary Sciences, **34**: 419-166.

Reniers, P., Farley, K., Hickes, H., 2—2. He Dfissuion and (U-Th)/He thermochronometry of

zircon: Initial results from Fish Canyon Tuff and Gold Butte, Nevada. Tectonophysics, **349**: 297-308.

Rivers, T. 1997. Lithotectonic elements of the Grenville Province: review and tectonic implications. Precambrian Research, **86**: 117-154.

Roden-Tice, M.K., West Jr., D.P., Potter, J.K., Raymond, S.M., Winch, J.L. 2009. Presence of a long-term lithospheric thermal anomaly: evidence from apatite fission-track analysis in northern New England. Journal of Geology, **117**: 627-641.

Roden-Tice, M.K., Wintsch, R.P. 2002. Early Cretaceous normal faulting in southern New England: evidence from apatite and zircon fission-track ages. Journal of Geology, **110**: 159-178.

Spotila, J.A., Bank, G.C., Reiners, P.W., Naeser, C.W., Naesert, N.D., Henika, B.S., 2004. Origin of the Blue Ridge escarpment along the passive margin of Eastern North America. Basin Research, **16**: 41-63.

Stea, R.R., Piper, D.J., Fader, G.B., Boyd, R. 1998. Wisconsinan glacial and sea-level history of Maritime Canada and the adjacent continental shelf: A correlation of land and sea events. GSA Bulletin, **110**: 821-845.

Stea, R.R., Pullan, S.E., 2001. Hidden Cretaceous basins in Nova Scotia. Canadian Journal of Earth Sciences, **38**: 1335-1354.

Stockli, D.F. 2005. Application of low temperature thermochronology to extensional tectonic settings. Reviews in Mineralogy and Geochemistry, 58: 411-448.

Stockli, D.F., Wolf, M.R. 2010. Zircon (U-Th)/He thermochronometry in the KTB drill hole, Germany- implications for the He diffusion in zircon. Earth and Planetary Science Letters, **295**: 69-82.

Taylor, J.P., Fitzgerald, P.G. 2011. Low-temperature thermal history and landscape development of the eastern Adirondack Moutains, New York: constraints from apatite fission-track thermochronology and apatite (U-Th)/He dating. Geological Society of America Bulletin, **123**: 412-246.

Waldron, J.W., White, C.E., Barr, S.M., Simonetti, A., Heaman, L. M. 2009. Provenance of the Meguma terrane, Nova Scotia: rifted margin of early Paleozoic Gondwana. Canadian , Journal of Earth Sciences, **46**: 1-8.

West Jr., D.P., Rowden-Tice, M.K., Potter, J.K., Barnard, N.Q. 2008. Assessing the role of orogeny-parallel faulting on post-orogenic exhumation: low temperature thermochronology across the Norumbega Fault System, Maine. Canadian Journal of Earth Science, **45**: 287-301.

White, C.E., SW Nova Scotia Bedrock [Map]. Scale: 1:50 000. Nova Scotia Department of Natural Resources 2012, ArcGIS.

Withjack, M.O., Schlische, R.W., Olsen, P.E. 2012. Development of the passive margin of Eastern North America: Mesozoic rifting, igneous activity and breakup in Roberts, D.G., and Bally, A.W., eds., Regional Geology and Tectonics, Volume 1B—Phanerozoic Rift Systems and Sedimentary Basins, New York, Elsevier, p. 301-335.

Withjack, M.O., Olsen, P.E., Schlische, R.W. 1995. Tectonic evolution of the Fundy rift basin,

Canada: Evidence of extension and shortening during passive margin development. Tectonics, **14**: 390-405.

Withjack, M.O., Schlische, R.W. 2005. A review of tectonic events on the passive margin of eastern North America. Petroleum Systems of Divergent Continental Margin Basins, 203-235.

Wolfe, M.R., Stockli. D.F. 2010. Zircon (U-Th)/He thermochronometry in the KTb drill hole. Germany, and its implications for bulk He diffusion kinetics in zircon. Earth and Planetary Science Letters, **295**: 69-82.

**Raw (U-Th[Sm])/He Data**

| Aliquot | mineral | mass, ug | UFt | ThFt | He, fmol | err., % | U, ng | err., abs. | Th, ng | err., abs. | 147Sm, ng | err., abs. | Th/U |
|---|---|---|---|---|---|---|---|---|---|---|---|---|---|
| aDUR-46 | apatite | 50 | 1.000 | 1.000 | 89.87132 | 1.86899 | 0.0971 | 0.00 | 1.8879 | 0.03 | 0.1150 | 0.01 | 19.43414227 |
| aCC01-1 | apatite | 2.499967 | 0.697 | 0.656 | 22.50117 | 1.88059 | 0.0363 | 0.00 | 0.0051 | 0.00 | 0.0340 | 0.00 | 0.140592905 |
| aCC01-2 | apatite | 4.539025 | 0.757 | 0.723 | 4.39084 | 1.91435 | 0.0023 | 0.00 | 0.0049 | 0.00 | 0.0206 | 0.00 | 2.147811302 |
| aCC01-3 | apatite | 5.618249 | 0.767 | 0.735 | 20.25918 | 1.88177 | 0.0315 | 0.00 | 0.0032 | 0.00 | 0.0088 | 0.00 | 0.102118655 |
| aCC01-4 | apatite | 4.643137 | 0.757 | 0.724 | 14.93186 | 1.88759 | 0.0169 | 0.00 | 0.0104 | 0.00 | 0.1018 | 0.01 | 0.61387624 |
| aCC01-5 | apatite | 1.860058 | 0.666 | 0.623 | 17.35387 | 1.88809 | 0.0265 | 0.00 | 0.0079 | 0.00 | 0.0209 | 0.00 | 0.297061117 |
| aCC03-1 | apatite | 4.20014 | 0.748 | 0.714 | 294.18853 | 1.86359 | 0.2823 | 0.00 | 0.0557 | 0.00 | 0.0878 | 0.00 | 0.197447884 |
| aCC03-2 | apatite | 1.67721 | 0.665 | 0.621 | 123.18825 | 1.86990 | 0.0869 | 0.00 | 0.0263 | 0.00 | 0.0494 | 0.00 | 0.302642891 |
| aCC03-3 | apatite | 3.207684 | 0.727 | 0.690 | 125.33067 | 1.86959 | 0.1499 | 0.00 | 0.0083 | 0.00 | 0.0620 | 0.00 | 0.055592012 |
| aCC03-4 | apatite | 2.135506 | 0.693 | 0.652 | 22.92035 | 1.87877 | 0.0299 | 0.00 | 0.0021 | 0.00 | 0.0303 | 0.00 | 0.071413044 |
| aCC03-5 | apatite | 2.60033 | 0.711 | 0.672 | 48.44981 | 1.88275 | 0.0628 | 0.00 | 0.0043 | 0.00 | 0.0397 | 0.00 | 0.068247008 |

**Appendix A: AHe and ZHe raw data**

**Raw (U-Th[Sm])/He Data**

| Aliquot | mineral | mass, ug | UFt | ThFt | He, fmol | err., % | U, ng | err., abs. | Th, ng | err., abs. | 147Sm, ng | err., abs. | Th/U |
|---|---|---|---|---|---|---|---|---|---|---|---|---|---|
| zFCT-15 | zircon | 15.29053 | 0.832 | 0.813 | 654.85059 | 1.82054 | 4.6471 | 0.06 | 3.2162 | 0.04 | 0.0000 | 0.00 | 0.692079389 |
| zCC01-1 | zircon | 20.88534 | 0.849 | 0.832 | ######### | 1.91439 | 12.9493 | 0.16 | 2.5199 | 0.05 | 0.2042 | 0.01 | 0.194599724 |
| zCC01-2 | zircon | 3.926797 | 0.748 | 0.720 | ######### | 1.92425 | 1.2415 | 0.01 | 0.2915 | 0.01 | 0.0019 | 0.01 | 0.234793038 |
| zCC01-3 | zircon | 6.737215 | 0.769 | 0.744 | ######### | 1.89492 | 5.4736 | 0.05 | 1.5704 | 0.03 | 0.1203 | 0.06 | 0.286897361 |
| zCC03-1 | zircon | 4.057759 | 0.754 | 0.726 | 666.98182 | 1.90931 | 0.6660 | 0.01 | 0.6303 | 0.01 | 0.0000 | 0.00 | 0.946466873 |
| zCC03-2 | zircon | 7.00573 | 0.784 | 0.760 | ######### | 1.90501 | 4.3773 | 0.11 | 0.8774 | 0.02 | 0.1974 | 0.17 | 0.200441125 |
| zCC03-3 | zircon | 6.776996 | 0.775 | 0.750 | ######### | 1.92379 | 2.4948 | 0.03 | 0.6201 | 0.01 | 0.0057 | 0.01 | 0.248567963 |
| zCC05-1 | zircon | 1.732556 | 0.681 | 0.646 | 553.04982 | 1.94607 | 0.0076 | 0.01 | 0.0004 | 0.00 | 0.0000 | 0.00 | 0.054021036 |
| zCC05-2 | zircon | 2.714957 | 0.726 | 0.696 | 531.47934 | 1.89807 | 0.5870 | 0.01 | 0.9525 | 0.01 | 0.0000 | 0.00 | 1.622560055 |
| zCC05-3 | zircon | 2.012863 | 0.683 | 0.648 | 404.55726 | 1.92268 | 0.3898 | 0.01 | 0.5738 | 0.01 | 0.0000 | 0.00 | 1.472116837 |
| zCC06-1 | zircon | 3.918264 | 0.751 | 0.724 | ######### | 1.89717 | 0.9606 | 0.01 | 0.5795 | 0.01 | 0.0000 | 0.00 | 0.603299997 |
| zCC06-2 | zircon | 4.494384 | 0.759 | 0.732 | ######### | 1.88473 | 0.8727 | 0.01 | 0.1907 | 0.00 | 0.0000 | 0.00 | 0.218552104 |
| zCC06-3 | zircon | 6.759038 | 0.786 | 0.762 | ######### | 1.77179 | 1.0954 | 0.02 | 0.3341 | 0.00 | 0.0000 | 0.00 | 0.304987922 |
| zCC07-1 | zircon | 15.37992 | 0.836 | 0.817 | ######### | 1.88624 | 2.1382 | 0.02 | 0.9163 | 0.01 | 0.0000 | 0.00 | 0.428548857 |
| zCC07-2 | zircon | 6.605281 | 0.775 | 0.750 | ######### | 1.89579 | 4.5620 | 0.05 | 0.8830 | 0.01 | 0.0011 | 0.02 | 0.193545147 |
| zCC07-3 | zircon | 7.758226 | 0.795 | 0.772 | ######### | 1.78503 | 1.2424 | 0.01 | 0.3057 | 0.00 | 0.0214 | 0.04 | 0.246017112 |

**Appendix B: Grain measurements and photos**

Apatite grains:

B1: CC01-1

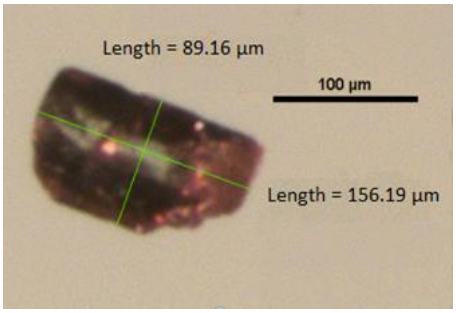


B2: CC01-2

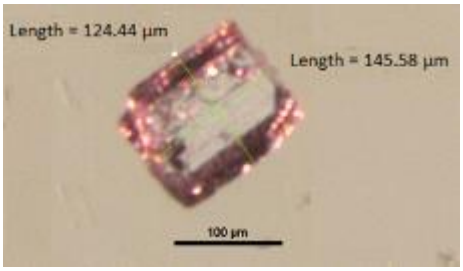


B3: CC01-3

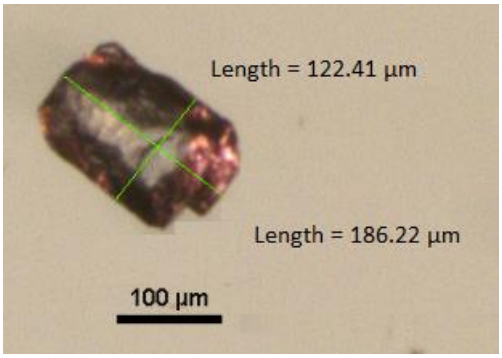


B4: CC01-4

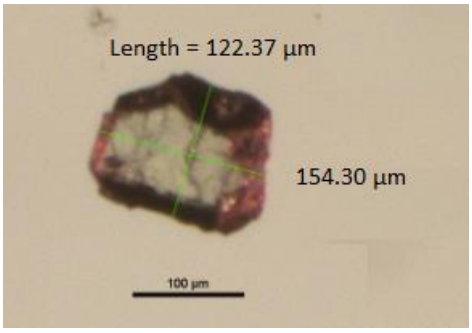


B5: CC01-5

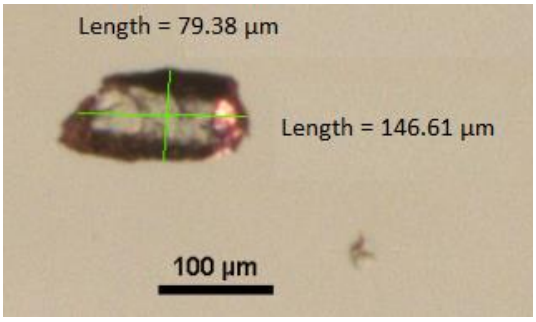


B6: CC03-1

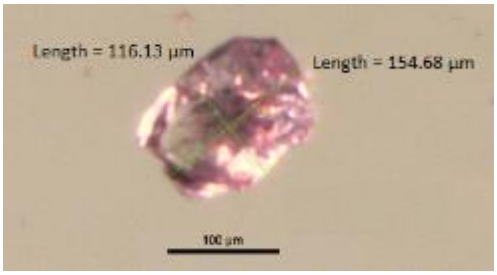


B7: CC03-2

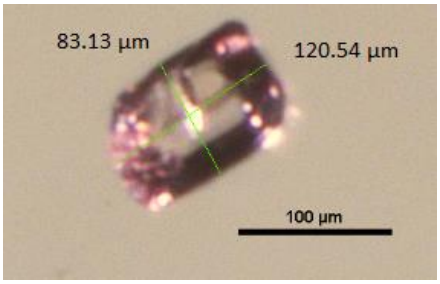


B8: CC03-3

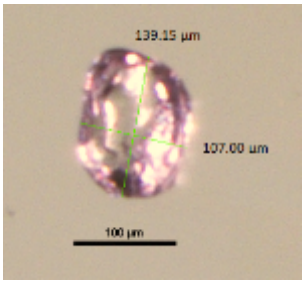


B9: CC03-4

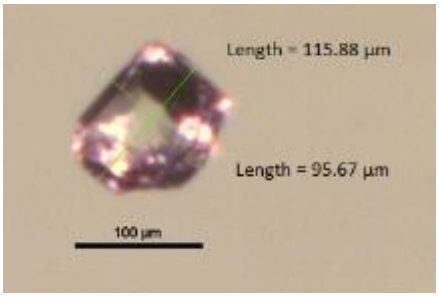


B10: CC03-5

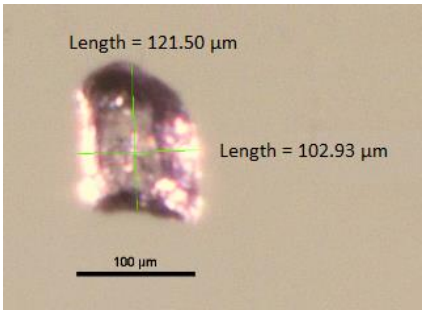


Zircon grains:

B11: CC01-1


B12: CC01-2

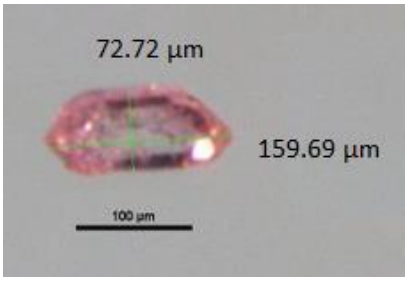


B13: CC01-3

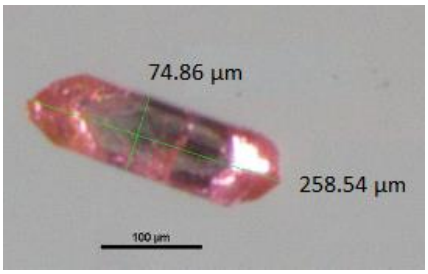


B14: CC03-1

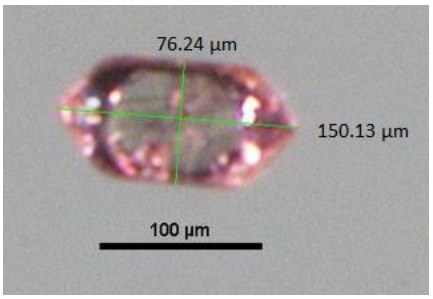

B15: CC03-2

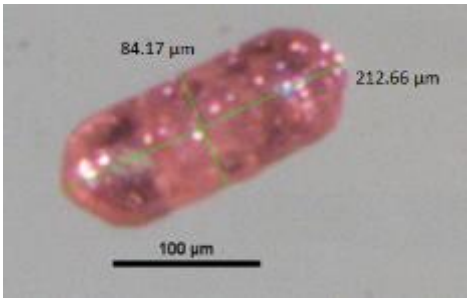


B16: CC03-3

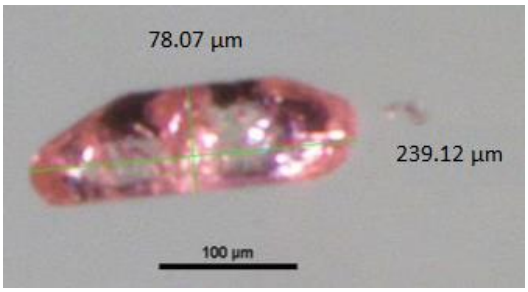


B17: CC05-1

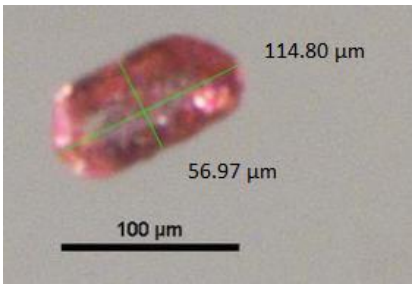


B18: CC05-2

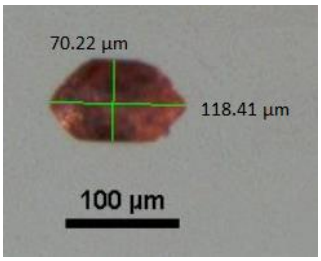


B19: CC05-3

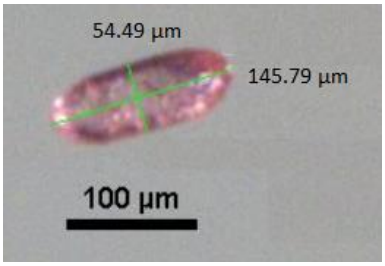


B20: CC06-1

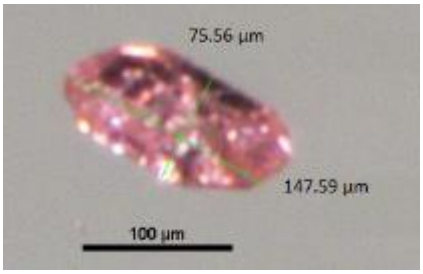


B21: CC06-2

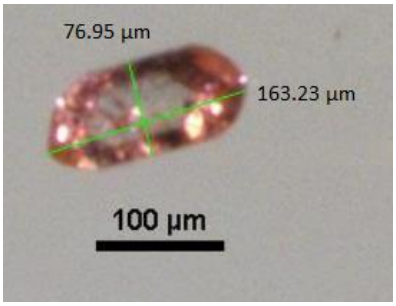


B22: CC06-3

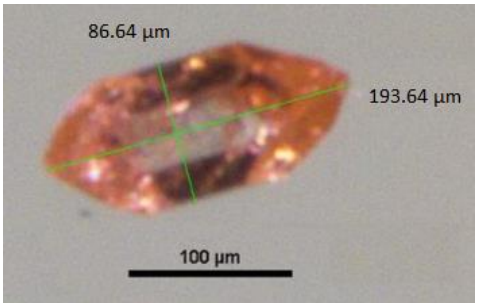


B23: CC07-1

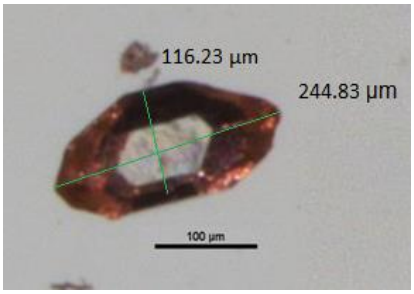


B24: CC07-2

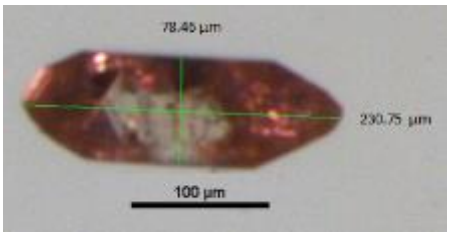


B25: CC07-3